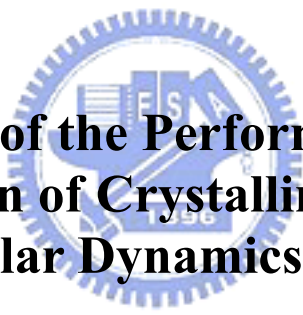


國立交通大學

機械工程學系

博士論文

以分子動力學研究結晶型太陽電池表面粗糙
化結構對效率之影響



**Investigation of the Performance for Surface
Texturization of Crystalline Solar Cells by
Molecular Dynamics Simulation**

研究生：鍾孝彥

指導教授：陳俊勳 博士
曲新生 博士

中華民國九十七年七月

以分子動力學研究結晶型太陽電池表面粗糙化結構
對效率之影響

Investigation of the Performance for Surface Texturization of
Crystalline Solar Cells by Molecular Dynamics Simulation

研究生：鍾孝彥

Student : Da-Ming Fan

指導教授：陳俊勳

Advisor : Chiun-Hsun Chen

曲新生

Hsin-Sen Chu



A Thesis

Submitted to Department of Mechanical Engineering

College of Engineering

National Chiao Tung University

in Partial Fulfillment of the Requirements

for the Degree of

DOCTOR OF PHILOSOPHY

in

Mechanical Engineering

July 2008

Hsinchu, Taiwan, Republic of China

中華民國九十七年七月

以分子動力學研究結晶型太陽電池表面粗糙化結構對效率之影響

學生：鍾孝彥

指導教授：陳俊勳 曲新生

國立交通大學

機械工程系

摘要

本研究藉由分子動力學的模擬，探討太陽電池表面粗糙化對太陽電池效率的影響。太陽電池的發電機制包含光子與電子、聲子的能量轉換，非常複雜。本研究發展了一個簡易的傳統分子動力學模型，以取代複雜的電子-光子-聲子的能量交換，藉以與拋光的太陽電池表面的理論效率做比較，求得各種粗糙化方式對結晶型太陽電池效率提升之量化指標。

本研究發現，無論是各種粗糙的形狀，當高低落差愈大，其效率提升愈高，若高低落差達到 14 埃，效率幾可提升 3 倍。若粗糙結構距離愈近，其效率提升愈高，距離縮小至 1 埃時，效率幾可比未做表面粗糙處理之太陽電池提升 2 倍。若將光的入射角度變化，則入射與垂直的夾角愈小，其效率愈高。

此外，若探討多晶態矽經鹼性溶液蝕刻後產生之金字塔型結構對太陽電池效率的影響，則因為金字塔角度的關係，會在某些角度範圍提昇轉換效率，但是其他角度則否；入射方位角改變亦會影響轉換效率；而金字塔角度愈大，則轉換效率愈提高。

在砷化鎵太陽電池方面，本研究採用 Tersoff 勢能模型與 Lennard-Jones 勢能模型之平均值來模擬原子與光子之間之交互作用，我們發現其趨勢類似於單晶矽太陽電池所得到之結果，當表面愈粗糙，其效率之提升愈大。

另一方面，我們也對原來的分子動力學模型做一些改進，根據前人的論文，聲子的傳遞對於光電效應的效率有重要的影響，因此我們加入了聲

子放射的概念。新的模型顯示，在平板太陽電池的光電轉換效率降低到 20 % 以下，表示一部份的能量被以熱的形式散失掉，但因此也更加接近太陽電池操作的實際狀況。同時降低聲子的傳遞可以使效率提升。這個結果也提供一個改進太陽電池效率的方向。

本文的研究，對於瞭解太陽電池表面粗糙化對效率的影響有很大的幫助。



Investigation of the Performance for Surface Texturization of Solar Cells by Molecular Dynamics Simulation

Student: Hsiao-Yen Chung

Advisor: Chiun-Hsun Cheng and Hsin-Sen Chu

**Department of Mechanical Engineering
National Chiao Tung University**

ABSTRACT

The purpose of this paper is to develop a simple new model, based on the classic molecular dynamics simulation (MD), alternative to complex electron-photon-phonon interactions to analyze the surface texturization of solar cells. This methodology can easily propose the absorptance differences between texturing and non-texturing solar cells. To verify model feasibility, this study simulates square, pyramidal, and semicircular texturization surfaces. Simulations show that surface texturization effectively increases the absorptance of incident light for solar cells, and this paper presents optimal texturization shapes. The MD model can also be potentially used to predict the efficiency promotion in any optical reflection-absorption cases.

In this study, we found higher drop of texturization increases the solar cells' efficiency. The closer distance of texturizations also increases the efficiency. The smaller incident angle also enhances the absorptance of solar cell to light.

Besides, in case of multi-crystalline silicon etching by alkaline solutions, the tilted angle of pyramids promotes the efficiency. Incident angle of light also affects the efficiency.

We also get a similar result in the case of GaAs solar cells. A new potential energy, the average of Tersoff potential model and Lennard-Jones potential model, was adapted to govern the interaction between GaAs atoms and photon. In this case, we also found the similar result as that from mono-crystalline silicon solar cell. The efficiency increased with the increase of GaAs solar cell surface's roughness.

We also appropriately modified our model with the concept of phonon emission. The absorptance that was higher than 60% decreased to almost 50%. Thus the results from the simulations with phonon emission were close to reality.

Besides, the results with phonon emission also lead to a new thought that the decreasing of heat loss can increase the efficiency of photovoltaic effect. In the mechanism of PV effect, decreasing phonon's transportation is one of feasible direction.

Our studies were helpful to realize the effect of surface texturization on the efficiency of crystalline solar cells.



誌 謝

首先誠摯的感謝恩師 曲新生 博士及 陳俊勳 博士。

因為家中事務的羈絆造成光陰的蹉跎，曲新生 老師對我仍然不放棄，除了在研究上悉心的指導與啟發，指點我正確的方向，並在生活及做人處事上多所指正我的缺失。老師對學問的嚴謹與為人處事的態度皆為我輩典範。

陳俊勳 老師的幫助，更是我能完成學業的重要推手。因為我的許多疏忽，造成 陳俊勳 老師的很多壓力，實在感銘五內。

其次感謝口試委員 陳朝光 老師、黃吉川 老師、陳慶耀 老師，以及本系熱流組 楊文美 老師等諸位教授對本論文的建議與指教，使本論文更加完整而嚴謹。

感謝 森溥 學長，總能在我迷惘時為我解惑。也感謝 純怡 學妹與 清益 學弟在課業上與生活上的協助。尤其感謝 式堯 學弟，在最後一年沒有任何援助之下，跟我一起孤軍奮戰，對我幫助極大。

非常感激家人的體諒與支持，在漫長的求學過程中，你們在背後的默默支持更是我前進的動力。

最後，謹以此論文，獻給含辛茹苦的母親大人，並告慰 父親大人的在天之靈。

TABLE OF CONTENTS

摘要	i
ABSTRACT.....	iii
TABLE OF CONTENTS.....	vi
LIST of FIGURES	viii
LIST of TABLES.....	xi
NOMENCLATURE	xii
1. Introduction.....	1
1.1. Background.....	1
1.1.1. History	1
1.1.2. Principles of solar cells.....	3
1.2 Literature Survey	9
1.2.1. Wet Etching.....	9
1.2.2. Dry etching	10
1.2.3. Molecular Dynamics Simulation on Photovoltaic issue	13
1.2.4. Heat Transfer Model using Molecular Dynamics Simulations	14
1.2. Objectives of Present Studies.....	17
2. Mathematical and Physical Model	26
2.1 The Molecular Dynamics Method	26
2.2 Predictor-Corrector Algorithms	28
2.3 Neighbor Lists.....	33

2.4 Model of Si and GaAs Solar Cells	34
2.5 Amorphous Silicon.....	36
2.6 Modified Model	37
2.7 Flow Chat of Calculation	38
3. Results and Discussion.....	53
3.1 Mono-crystalline Si solar cells.....	53
3.2 Multi-crystalline (mc) Si solar cells	54
3.3 GaAs Solar Cells.....	56
4. Modified Model with Phonon Emission	70
5. Conclusions and Recommendations	78
Reference	81

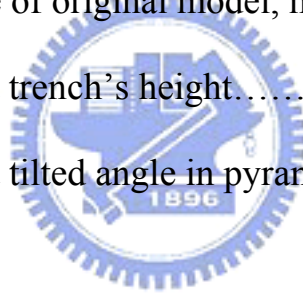


LIST of FIGURES

Fig 1-1. Silicon’s structure.....	18
Fig 1-2. Band diagram and the electron-hole distribution in semiconductors.....	19
Fig 1-3. Diagram of p-n junction formation and the resulting band structure.....	20
Fig 1-4. The I-V characteristic of a diode.....	21
Fig 1-5. The generation of electron-hole pairs by light.....	22
Fig 1-6. Photon flux utilized by a silicon solar cell.....	23
Fig 1-7. The process of manufacturing silicon solar cells.....	24
Fig 2-1. Illustrations of attractive and repulsive interaction of atoms and photons. (a) The photons moves toward repulsive force field are probably rebound out, and the other photons move through attractive field is constrained or decelerated. (b) The rebounded behavior is as same as reflection. The constraint behavior is as same as absorption.....	40
Fig 2-2. The structure of (a) silicon, and (b) GaAs.....	41
Fig 2-3. Physical Model (a) square (b) pyramid (c) semicircle, the geometric variables are also shown in this figure.....	42
Fig 2-4. The model of mc-silicon by alkaline etching. The tilted angle is α ...44	44
Fig 2-5. Verlet List.....	45

Fig 2-6. The process to form amorphous substrate.....	46
Fig 2-7. The model of phonon emission.....	47
Fig 2-8. Flow Chart.....	48
Fig 3-1. The relation among absorptance, h and photon's incidence angle θ of mono-crystalline silicon.....	58
Fig 3-2. The relation among absorptance, distance and photon's incidence angle θ of mono-crystalline silicon.....	59
Fig 3-3. The relation among absorptance, facet titled angle α and photon' incidence angle θ of mono-crystalline silicon.....	60
Fig 3-4. The dependence of absorptance on H/r in the case of semicircular texturing surface of mono-crystalline silicon.....	61
Fig 3-5. Schematic illustration of reflection on the surface of mc-silicon after alkaline etching.....	62
Fig 3-6. The relation of absorptance and the tilted angle, agreeing with the result of Xi <i>et al.</i> [1].....	63
Fig 3-7. The relation of absorptance and incident angle.....	64
Fig 3-8. The position of the triangle of principal orientations. The incident angle θ and the azimuth angle φ are demonstrated.....	65
Fig 3-9. The relation between the azimuth angle φ and absorptance.....	66
Fig 3-10. The relation among absorptance, h and photon's incidence angle θ of GaAs.....	67

Fig 3-11. The relation among absorptance, distance and photon's incidence angle θ of GaAs.....	68
Fig 3-12. the absorptance comparison of amorphous substrate and crystalline substrate in the case of height of square texturing for the square surface case.....	69
Fig 4-1. Three models of Lennard-Jones potential. Model 1 is a regular distance effect, and model 2 is shorter distance and model 3 is longer distance.....	73
Fig 4-2. Absorptance via numbers of cells.....	74
Fig 4-3. The absorptance of original model, model 1, 2 and 3.....	75
Fig 4-4. Absorptance via trench's height.....	76
Fig 4-5. Absorptance via tilted angle in pyramidal surface texturization.....	77



LIST of TABLES

Table 1-1. The bandgaps of the most important semiconductors for solar-cell applications.....	25
Table 2-1. The physical parameters of silicon and GaAs.....	49
Table 2-2. The parameters of Tersoff potential for GaAs.....	50
Table 2-3. Values of α_i parameters in Gear's Predictor-Corrector Algorithm for second-order differential equations using predictors of order q	51
Table 2-4. Speed of Execution of Lennard-Jones Program with and without Neighbor List.....	52



NOMENCLATURE

- a : accelation [m/s^2]
- C : heat capacity [J/kg-k]
- E : energy
- f : cut off function
- F : force
- h : Plank's constant [J s]
- \hbar : $h/2\pi$ [J s]
- k : heat transfer coefficient [W/m-K]
- k_B : Boltzmann Constant [J/K]
- m : phonon moduii
- N : Numbers of particles
- r : distance between particles
- t : time step
- T : system temperature [K]
- θ_a : nondimensional temperature
- U : Potential energy
- v : velocity [m/s^2]
- V : volume [m^3]
- q : heat flux [W/m^2]
- Q : total heat flux [W]

Greek

α : tilted angle [degree]

λ : phonon wavelength [m]

θ, ϕ : incident angle [degree]

φ : azimuth angle [degree]

τ : relaxation time [s]

ω : frequency [1/s]

ρ : density [kg/m³]

Λ : mean free path[m]

Superscripts

i, j, k : the i, j, k -th particle

Subscripts

P : predictor

C : corrector



1. Introduction

The solar cell is a photovoltaic device designed to convert sunlight directly into electrical power and to deliver this power to a suitable load in an efficient manner. Solar energy has a very desirable property of being essentially limitless without encountering the problems of pollution or physical danger.

1.1. Background

1.1.1. History

The term "photovoltaic" comes from the Greek $\phi\acute{o}\varsigma$ (*phos*) meaning "light", and "voltaic", meaning electrical, from the name of the physicist, after whom the measurement unit is named. The term "photo-voltaic" has been in use in English since 1849.

The photovoltaic effect was first recognized by French physicist. In 1839, as he was experimenting with an electrolytic cell composed of two metal electrodes, Edmund Becquerel discovered the photovoltaic effect[2]. In 1876, William Adams and Richard Day[2] found that a sample of selenium contacted by two heated platinum contact could produce a photo current.

However, it was not until that the first solar cell was built, by Charles Fritts, who coated the semiconductor selenium with an extremely thin layer of gold to form the junctions [3]. The device was only around 1% efficient. Russell Ohl [2] patented the modern solar cell in 1946 (U.S. Patent 2,402,662 , "*Light sensitive device*"). Sven Ason Berglund [2] had a prior patent concerning methods of increasing the capacity of photosensitive cells. The modern age of solar power technology arrived in 1954 when Daryl Chapin, Calvin Fuller and Gerald

Pearson of Bell Laboratories, experimenting with semiconductors, accidentally found that silicon doped with certain impurities was very sensitive to light [4, 5].

This resulted in the production of the first practical solar cells with a sunlight energy conversion efficiency of around 6 percent. Russia launched the first artificial satellite in 1957, and the United States' first artificial satellite was launched in 1958 using solar cells created by Peter Iles in an effort spearheaded by Hoffman Electronics. The first spacecraft to use solar panels was the US satellite Explorer 1 in January 1958. This milestone created interest in producing and launching a geostationary communications satellite, in which solar energy would provide a viable power supply. This was a crucial development which stimulated funding from several governments into research for improved solar cells.

In 1970 the first highly effective GaAs heterostructure solar cells were created by Zhores Alferov and his team in the USSR [6, 7]. Metal Organic Chemical Vapor Deposition (MOCVD, or OMCVD) production equipment was not developed until the early 1980's, limiting the ability of companies to manufacture the GaAs solar cell. In the United States, the first 17% efficient air mass zero (AM0) single-junction GaAs solar cells were manufactured in production quantities in 1988 by Applied Solar Energy Corporation (ASEC). The "dual junction" cell was accidentally produced in quantity by ASEC in 1989 as a result of the change from GaAs on GaAs substrates to GaAs on Germanium (Ge) substrates. The accidental doping of Ge with the GaAs buffer layer created higher open circuit voltages, demonstrating the potential of using the Ge substrate as another cell. As GaAs single-junction cells topped 19% AM0 production efficiency in 1993, ASEC developed the first dual junction cells for spacecraft use in the United States, with a starting efficiency of approximately 20%. These cells did not utilize the Ge as a second cell, but used another GaAs-based cell with different doping. Eventually GaAs dual junction cells reached production efficiencies of about

22%. Triple Junction solar cells began with AM0 efficiencies of approximately 24% in 2000, 26% in 2002, 28% in 2005, and in 2007 have evolved to a 30% AM0 production efficiency, currently in qualification. In 2007, two companies in the United States, Emcore Photovoltaics and Spectrolab, produce 95% of the world's 28% efficient solar cells.

1.1.2. Principles of solar cells

The principles of semiconductor physics are best illustrated using the example of silicon, a group 4 elemental semiconductor, shown in figure 1-1. The silicon crystal forms the so-called diamond lattice where each atom has four nearest neighbors at the vertices of a tetrahedron. The four-fold tetrahedral co-ordination is the result of the bonding arrangement which uses the four outer (valence) electrons of each silicon atom. Each bond contains two electrons, and you can easily see that all the valence electrons are taken up by the bonds. Most other industrially important semiconductors crystallise in this or closely related lattices, and have a similar arrangement of the bonding orbital.

This crystal structure has a profound effect on the electronic and optical properties of the semiconductor. According to the quantum theory, the energy of an electron in the crystal must fall within well-defined bands. The energies of valence orbitals which form bonds between the atoms represent just such a band of states, the valence band. The next higher band is the conduction band which is separated from the valence band by the energy gap, or bandgap. The width of the bandgap $E_c - E_v$ is a very important characteristic of the semiconductor and is usually denoted by E_g . The table 1-1 gives the bandgaps of the most important semiconductors for solar-cell applications.

Figure 1-2 gives the band diagram and electron-hole distribution. A pure semiconductor (which is called intrinsic) contains just the right number of electrons to fill the valence band,

and the conduction band is therefore empty. Electrons in the full valence band cannot move - just as, for example, marbles in a full box with a lid on top. For practical purposes, a pure semiconductor is therefore an insulator.

Semiconductors can only conduct electricity if carriers are introduced into the conduction band or removed from the valence band. One way of doing this is by alloying the semiconductor with an impurity. This process is called doping. As we shall see, doping makes it possible to exert a great deal of control over the electronic properties of a semiconductor, and lies in the heart of the manufacturing process of all semiconductor devices.

Suppose that some group 5 impurity atoms (for example, phosphorus) are added to the silicon melt from which the crystal is grown. Four of the five outer electrons are used to fill the valence band and the one extra electron from each impurity atom is therefore promoted to the conduction band. For this reason, these impurity atoms are called donors. The electrons in the conduction band are mobile, and the crystal becomes a conductor. Since the current is carried by negatively charged electrons, this type of semiconductor is called n type.

A similar situation occurs when silicon is doped with group 3 impurity atoms (for example, boron) which are called acceptors. Since four electrons per atoms are needed to fill the valence band completely, this doping creates electron deficiency in this band. The missing electrons - called holes - behave as positively charged particles which are mobile, and carry current. A semiconductor where the electric current is carried predominantly by holes is called p-type.

The operation of solar cells is based on the formation of a junction, shown in figure 1-3. The important feature of all junctions is that they contain a strong electric field. To illustrate how this field comes about, let us imagine the hypothetical situation where the p-n junction is

formed by joining together two pieces of semiconductor, one p-type and the other n-type. In separation, there is electron surplus in the n-type material and hole surplus in the p-type. When the two pieces are brought into contact, electrons from the n region near the interface diffuse into the p side, leaving behind a layer which is positively charged by the donors. Similarly, holes diffuse in the opposite direction, leaving behind a negatively charged layer stripped of holes. The resulting junction region then contains practically no mobile charge carriers, and the fixed charges of the dopant atoms create a potential barrier acting against a further flow of electrons and holes. Note that the electric field in the junction pulls the electrons and holes in opposite directions.

The potential barrier of a junction permits the flow of electric current in only one direction - the junction acts as a rectifier, or diode. This can be seen in our example where electrons can only flow from the p region to the n region, and holes can only flow in the opposite direction. Electric current, which is the sum of the two, can therefore flow only from the p-side to the n-side of the junction. The I-V characteristic of a diode is shown in figure 1-4.

Photovoltaic energy conversion relies on the quantum nature of light whereby we perceive light as a flux of particles called photons. On a clear day, about 4.4×10^{17} photons strike a square centimeter of the Earth's surface every second.

Only some of these photons - those with energy in excess of the bandgap - can be converted into electricity by the solar cell. When such photon enters the semiconductor, it may be absorbed and promote an electron from the valence to the conduction band. Since a hole is left behind in the valence band, the absorption process generates electron-hole pairs, shown in figure 1-5.

Each semiconductor is restricted to converting only a part of the solar spectrum. The spectrum is plotted in figure 1-6 in terms of the incident photon flux as a function of photon energy. The shaded area represents the photon flux that can be converted by a silicon cell - about two-thirds of the total flux.

The nature of the absorption process also indicates how a part of the incident photon energy is lost in the event. Indeed, it is seen that practically all the generated electron-hole pairs have energy in excess of the bandgap. Immediately after their creation, the electron and hole decay to states near the edges of their respective bands. The excess energy is lost as heat and cannot be converted into useful power. This represents one of the fundamental loss mechanisms in a solar cell.

Because solar cells are semiconductor devices, they share many of the same processing and manufacturing techniques as other semiconductor devices such as computercom and memory chips. However, the stringent requirements for cleanliness and quality control of semiconductor fabrication are a little more relaxed for solar cells. Most large-scale commercial solar cell factories today make screen printed poly-crystalline silicon solar cells. Single crystalline wafers which are used in the semiconductor industry can be made into excellent high efficiency solar cells, but they are generally considered to be too expensive for large-scale mass production.

Figure 1-7 shows the process of manufacturing solar cells. Generally, the first step is making texturization on the surface of a silicon wafer. Then dopants diffuse to the wafer. Coating reflection layers is processed after removing the glass layer, produced by oxidation effects, on the surface of wafer. Then the silk screen printing, oven firing and efficiency testing is made.

Poly-crystalline silicon wafers are made by wire-sawing block-cast silicon ingots into very thin (180 to 350 micrometer) slices or wafers. The wafers are usually lightly p-type doped. To make a solar cell from the wafer, a surface diffusion of n-type dopants is performed on the front side of the wafer. This forms a p-n junction a few hundred nanometers below the surface.

Antireflection coatings, which increase the amount of light coupled into the solar cell, are typically applied next. Over the past decade, silicon nitride has gradually replaced titanium dioxide as the antireflection coating of choice because of its excellent surface passivation qualities (i.e., it prevents carrier recombination at the surface of the solar cell). It is typically applied in a layer several hundred nanometers thick using plasma-enhanced chemical vapor deposition (PECVD). Some solar cells have textured front surfaces that, like antireflection coatings, serve to increase the amount of light coupled into the cell. Such surfaces can usually only be formed on single-crystal silicon, though in recent years methods of forming them on multicrystalline silicon have been developed.

The wafer is then metallized, whereby a full area metal contact is made on the back surface, and a grid-like metal contact made up of fine "fingers" and larger "busbars" is screen-printed onto the front surface using a silver paste. The rear contact is also formed by screen-printing a metal paste, typically aluminium. Usually this contact covers the entire rear side of the cell, though in some cell designs it is printed in a grid pattern. The paste is then fired at several hundred degrees Celsius to form metal electrodes in ohmic contact with the silicon. After the metal contacts are made, the solar cells are interconnected in series (and/or parallel) by flat wires or metal ribbons, and assembled into modules or "solar panels". Solar panels have a sheet of tempered glass on the front, and a polymer encapsulation on the back.

Tempered glass cannot be used with amorphous silicon cells because of the high temperatures during the deposition process.

The solar cell was firstly developed by Chapin, Fuller, and Pearson in 1954 using a diffused silicon p-n junction[4]. Subsequently, the cadmium-sulfide solar cell was developed by Reynolds *et al.*[8] Historically, silicon was the first commercially used for the solar cell material and it is the most extensively studied semiconductor in the present day. To date, solar cells have been made in many other semiconductors, using various device configurations with high-purity silicon and optimized solar cell designs, the efficiencies of 23% can be experimentally achieved under normal sunlight.[9] However, the polycrystalline silicon used in the commercial cells and modules, the efficiencies of about 17% are now obtained[10].

A wide variety of compound semiconductor, such as GaAs, InP, CdTe, and CdS, which have a band gap that is more suitable to the sunlight spectrum and therefore is potential for high efficiency. Especially, III-V compound semiconductors are used for space solar cells, concentrator solar cells, and thermophotovoltaic generators. Recent studies of GaAs solar cells have even demonstrated the efficiencies of about 25%[11-14].

Generally speaking, optical losses in solar cells originate from the three major reasons: surface reflection, top grid shadowing, and inadequate absorption, illuminated by either excess energy photons or weak energy photons. So these three directions are deserved to be explored.

According to the manufacturing process, shown in figure 1-7, surface texturization is an important key to lower surface reflection so that my study is focused on this problem.

1.2 Literature Survey

Achieving higher efficiency in solar cells is the one of most important issues in recent studies on the topic, and researchers have examined many methods for achieving this goal. Surface texturing of solar cells is a common approach to reduce incident light reflection and, consequently, increase solar cell efficiency.

1.2.1. Wet Etching

Wet etching means surface texturing with chemical solutions. In a general surface texturing process on crystalline silicon, alkaline solutions form pyramids. This pyramidal surface shape occurs because alkaline solutions etch silicon along crystallographic orientations.

Some researchers use acid solutions to produce surface texturization. Due to the character of acid solutions, the etching rates in the different orientations are similar. Thus a semicircular structure is formed[15].

Most texturing studies focus on wet etching processes. Hylton *et al.* [16] conducted many experiments to compare the efficiency increase of saw-damage etching and texture etching processes using alkaline solutions on multicrystalline silicon wafers. That paper also explained the geometrical paths of incident light which defined the absorption and reflection on the pyramid structures. Nishimoto and Namba[17] developed a low-cost wet etching manufacturing process and reported the texturization of a monocrystalline silicon surface with low cost alkaline solutions, Na_2CO_3 . Recently, Gangopadhyay and his colleagues[18] further developed a new texturing method with tribasic sodium phosphate solution, claiming it was superior to the conventional method because it used less isopropyl alcohol for texturing.

New solutions are also applied. Marrero *et al.* [19] describes a texturization method for monocrystalline silicon solar cells based on a mixture of sodium carbonate and sodium hydrogen carbonate solutions. A specific solution has been found that results in an optimal etching rate, the lowest surface reflectance and a homogeneous density of pyramidal structures on the silicon surface. The subsequent phosphorus diffusion with rapid thermal processes has been modified in order to drastically reduce the process time and, simultaneously, to obtain a high homogeneity of the sheet resistance values and improved photocarriers lifetimes. 100×100 mm solar cells with an efficiency of 15.8% have been obtained compared to an efficiency of 14.7% for the reference cell.

Usual step during PV cell production is surface texturization, which is performed to reduce the reflection losses from the front surface of solar cells. Conventional chemical and electrochemical methods are efficient in texturing monocrystalline silicon [15]. Unfortunately, these methods are inefficient for multicrystalline silicon due to the presence of random crystallographic grain orientations and high selectivity of etching along specific directions. Consequently, it is impossible to obtain texturization of homogeneous structure on the whole surface [20-24]. Another possibility is mechanical texturization [25]. Unfortunately, it is also not satisfactory due to possible mechanical damages, resulting in breakability and fragility of silicon and additionally very small thickness of silicon wafers. Therefore, there is a real need for a versatile, gentle process that is capable of producing the layer of regular texture. The possible way of overcoming these difficulties is laser texturization [22, 26, 27]

1.2.2. Dry etching

Dry etching and the wet etching are commonly used to apply surface texturization to solar cells. Dry etching means texturing without wet solutions. A selective surface texturing technique using lasers recently gained some interest.

Nowadays, lasers of different types are used in a variety of material processing applications for a wide range of materials [28]. They have been applied in processes including welding, cutting, drilling, grooving, ablation deposition and surface treatment. Nd-YAG laser can be successfully used for surface treatment of multicrystalline silicon. Both continuous wave and pulsed light lasers can be applied in material processing. Since laser material processing is a process that involves many physical phenomena such as:

- transmission, absorption, and reflection of radiant energy,
- conduction, convection, and radiation of thermal energy,
- melting and solidification,
- vaporization,

the selection of appropriate process parameters guaranteeing the achievement of demanded texture is generally difficult[26].



A selective surface texturing technique using lasers recently gained some interest. Tan *et al.*[29] performed femtosecond pulsed laser induced forward transfer on a quartz substrate. A trench-like texturing was ablated on the donor substrate using a pulsed laser. This method exhibits good controls on the depth and width of ablated trenches. Dobrzanski *et al.* [28] design the technique of laser texturization for solar cells made of multicrystalline silicon and improve understanding of the interaction between laser light and workpiece. They explore how different transverse modes influence laser surface treatment and examine some details related to laser multimodal operation. Since constant increase in global production of photovoltaic power can be observed the new technologies for manufacturing solar cells of improved efficiency are developed. One of the most important factors influencing cells performance is reflectivity of its front side. Consequently, new methods for efficient reduction

of reflectance are searched. One of the crucial stages which are carried out to increase solar radiation absorption is surface texturization. It is brought under well control for solar cells made of monocrystalline silicon. However, from the market point of view the reduction of production costs has essential meaning. As a result, the market share of multicrystalline cells systematically grows since the base material is approximately twice cheaper compared to monocrystalline silicon. But on the other hand, texturization methods used for monocrystalline silicon are ineffective in the case of multicrystalline silicon. Thus, it seems to be very interesting to investigate new alternative methods for effective texturization of multicrystalline silicon.

Besides, a plasma texturing technique using reactive ion etching, with advantages of low cost consumption and independence from crystallographic orientation, was previously proposed[24, 30]. Texturing by reactive ion etching (RIE) has recently gained wide-spread interest. Specifically results published by the *Kyocera* group for crystalline solar cells in 1996 [31-33] stimulated activities world wide. Etch processes that are independent of crystallographic orientation appear most attractive. In addition, low consumption of silicon as well as the advantage of a contact-free process plays an increasing importance in cell production. The low-cost potentials inherent stimulate further interest in industrial applications.

Beside RIE with auto-masking by metal evaporation, texturization by “natural lithography” has been proposed as possible solution. RIE by natural lithography is a texturing method based on colloidal particle masking. It was first published by Deckman and Dunsmuir in 1982 [34]. One clear advantage of this method is the ability to control lateral periodicity of the mask via particle size. A second advantage is that standard etch processes can be used; no modification of industrial etch procedures in order to achieve auto-masking is required. On

the other hand, compared to maskless texturization processes additional process steps for mask preparation and removal are required. The problem of consecutive homogeneity is transferred to the preparation of the mask.

Nositschka *et al.* [35] recently developed a suitable sequence of processes to combine the advantage of reactive ion etching with “natural lithography” based on colloidal masks. The RIE single-wafer texturization in this paper is driven to an industrial applicable batch process by plasma etching with a gain in efficiency of 0.3% absolute.

1.2.3. Molecular Dynamics Simulation on Photovoltaic issue

Molecular dynamics simulation is a technique well suited to nanoscale phenomena and mechanical behaviors [36-38]. However, few studies use MD to examine solar-cell issues. Stir *et al.* [37] explores the photo-induced electron-transfer phenomena on a dye sensitized titanium solar cell with non-adiabatic MD simulations (NAMMD), which is based on the *ab-initio* functional theory. The system under study is typical of the dye sensitized semiconductor nanomaterials used in solar cells, photocatalysis and photoelectrolysis. The electronic structure of the dye-semiconductor system and the adiabatic dynamics are simulated by *ab initio* density functional theory MD, while the NA effects are incorporated by the quantum-classical mean-field approach. A novel procedure separating the NA and adiabatic ET pathways is developed. The simulation provides a detailed picture of the ET process. For the specific system under study, ET occurs on a 30 fs time scale, in agreement with the ultrafast experimental data. Both adiabatic and NA pathways for the ET are observed. The NA transfer entirely dominates at short times and can occur due to strong localized avoided crossing as well as extended regions of weaker NA coupling. Although the adiabatic ET contribution accumulates more slowly, it approaches that of the NA ET pathway asymptotically. The electron acceptor states are formed by the d-orbital of Ti atoms of the

semiconductor and are localized within the first 3-4 layers of the surface. About 20% of the acceptor state density is localized on a single Ti atom of the first surface layer. The simulation predicts a complex non-single-exponential time dependence of the ET process.

However, many unknown factors in photon-electron interactions prevent studies from being conducted on the issue of photon absorption. On the other hand, this issue is deserved to study.

1.2.4. Heat Transfer Model using Molecular Dynamics Simulations

Heat conduction in dielectric materials is dominated by lattice vibration under Debye temperature. The phonons, in which these vibration energies named, are transport among atoms and produce scattering with another phonons electrons, impurities and geometric boundaries. If the mean free path (MFP) is smaller than the characteristic sizes of materials, the transport process is diffusion-like. Thus the Fourier Law of heat conduction can describe this behavior. While the MFP of phonons is significantly longer than the size, which means a very tiny material is considered, local thermal dynamic non-equilibrium exists in this material, the classical diffusion-like Fourier Law can not govern this phenomenon any more, therefore microscopic theories and techniques must be developed to govern these phenomena of heat transport in microscale materials [39-41].

In microscopic theories, the molecular dynamics method (MD) is a better technique to measure thermal conductivity in nanoscale materials [42]. This method simulated the movement of particles (atoms or molecules) in materials by solving Newton's second motion law, in which the force is given from a specific potential function between two (or among three) particles. The thermal dynamic and transport properties of this system can be derived by using some related statistical equations [43]. The pioneers to study this problem are Kotake

and Waruki [44]. They measured heat conduction in argon-type solid by MD simulation and clearly described the temperature gradient between layers of temperature difference. In order to investigate the transient heat flow in solids, Volz *et al.* [45, 46] computed the characteristic phonon mean relaxation time, the heat flux relaxation time, and the hydrodynamics time in a high-density argon crystal by conducting MD simulation. Maiti *et al.* [47] estimated the requisites for establishing local thermodynamic equilibrium in NEMD simulations and the Kapitza thermal boundary resistance that arises from heat flow across Si grain boundaries. Volz *et al.* [48] furthermore examined the thermal conductivity of single-crystal silicon nanowires based on MD simulations. It was shown that thermal conductivities of one-dimensional nano materials could be about two orders of magnitude smaller than those of bulk crystals. In recent study, they also reported the heat transfer in Si/Ge ultra-thin film multilayers by MD techniques and the Green-Kubo formula, which is derived from the fluctuation-dissipation theorem to calculate thermal conductivity [49, 50]. Feng *et al.*[51] studied the size effect of lattice thermal conductivity across nanoscale thin films of argon at relatively high temperature. They found the size effect of thermal conductivity can be detected in the normal direction in films with a thickness of 2 ~10 nm at an average temperature of about $T=1.3\theta_D$ (about 89.85K, θ_D is Debye temperature). The thin film conductivity is observably lower than its bulk counterpart as well as shows monotonous dependency on film thickness, and the results from Boltzmann Transport Equation (BTE) are shown to be in fair agreement with the MD results when the specular reflectivity of phonons at film boundaries $p=0.205$ is chosen. The aforementioned studies have demonstrated the validity and feasibility of exploring heat conduction properties of solids by using MD simulations, and revealed the distinction of thermophysical properties between nanoscale and bulk materials. However, most of these studies explored thermal conductivity in only one crystalline form. The effects of materials' structure on thermal conductivity are lack of discussion. Thus some researchers

recently took notice of the affects of crystalline forms on energy transport. In 2002, Hiroasaki *et al.* [52] are the first to study this subject. They explored thermal conductivities of α - and β -Si₃N₄ by MD calculation and Green-Kubo formulation. They found that the thermal conductivity could be estimated with a high degree of accuracy. The calculated elastic constants of the crystals were compared with the Slack's equation and found to be in reasonable.

Furthermore, A. J. Nozik[53] mentioned the major factor limiting the conversion efficiency in single band gap cells is that the absorbed photon energy above the semiconductor band gap is lost as heat through electron-phonon scattering and subsequent phonon emission, as the carriers relax to their respective band edges (bottom of conduction band for electrons and top of valence for holes). The main approach to reduce this loss in efficiency has been to use a stack of cascaded multiple p-n junctions with band gaps better matched to the solar spectrum; in this way higher-energy photons are absorbed in the higher-band-gap semiconductors and lower-energy photons in the lower-band-gap semiconductors, thus reducing the overall heat loss due to carrier relaxation via phonon emission. In the limit of an infinite stack of band gaps perfectly matched to the solar spectrum, the ultimate conversion efficiency at one sun intensity can increase to about 66%.

Another approach to increasing the conversion efficiency of photovoltaic cells by reducing the loss caused by the thermal relaxation of photogenerated hot electrons and holes is to utilize the hot carriers before they relax to the band edge via phonon emission [54]. There are two fundamental ways to utilize the hot carriers for enhancing the efficiency of photon conversion. One way produces an enhanced photovoltage, and the other way produces an enhanced photocurrent [55-58].

However, we noted that the efficiency of solar cells is relative to the interaction among photons, electrons and phonons. So this is a direction that we can make more research.

1.2. Objectives of Present Studies

The above literature review shows that there is still much necessity to investigate the problem of enhancing solar cells' efficiency. Also, the relations of surface texturization effects are still not well understood. In this study, a simple photon-atomic model with molecular dynamics simulations to explore the effects solar cell surface texturization is developed and numerically solved to enhance the understanding of the underlying characteristics of different shapes of surface texturization by wet or dry etching.

The scopes of this investigation are mainly focused on three parts. Firstly, we develop a simple molecular dynamics model with Lennard Jones potential model to explore the relations of surface texturization and absorptance. The possible shapes of texturization, such as square, pyramid and semicircular texturizations, are simulated in one-dimensional various incident light. Secondly, a real-closely pyramid texturization on the surface of multi-crystalline silicon substrate etching by alkaline solutions is simulated by the same molecular dynamics model to explore the influences of incident, azimuth and tilted angles with absorptance. Finally, GaAs and amorphous substrate is explored with the same model.

Following this concept, we then modified this model with phonon emission to approach the real PV transform in a PV solar cell.

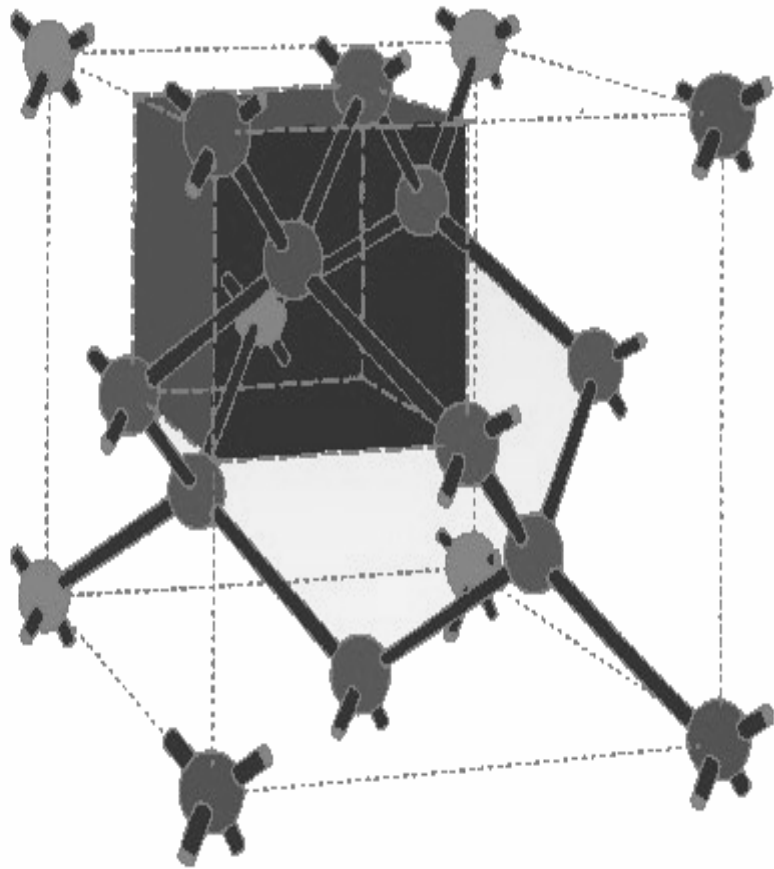


Fig. 1-1 Silicon's structure

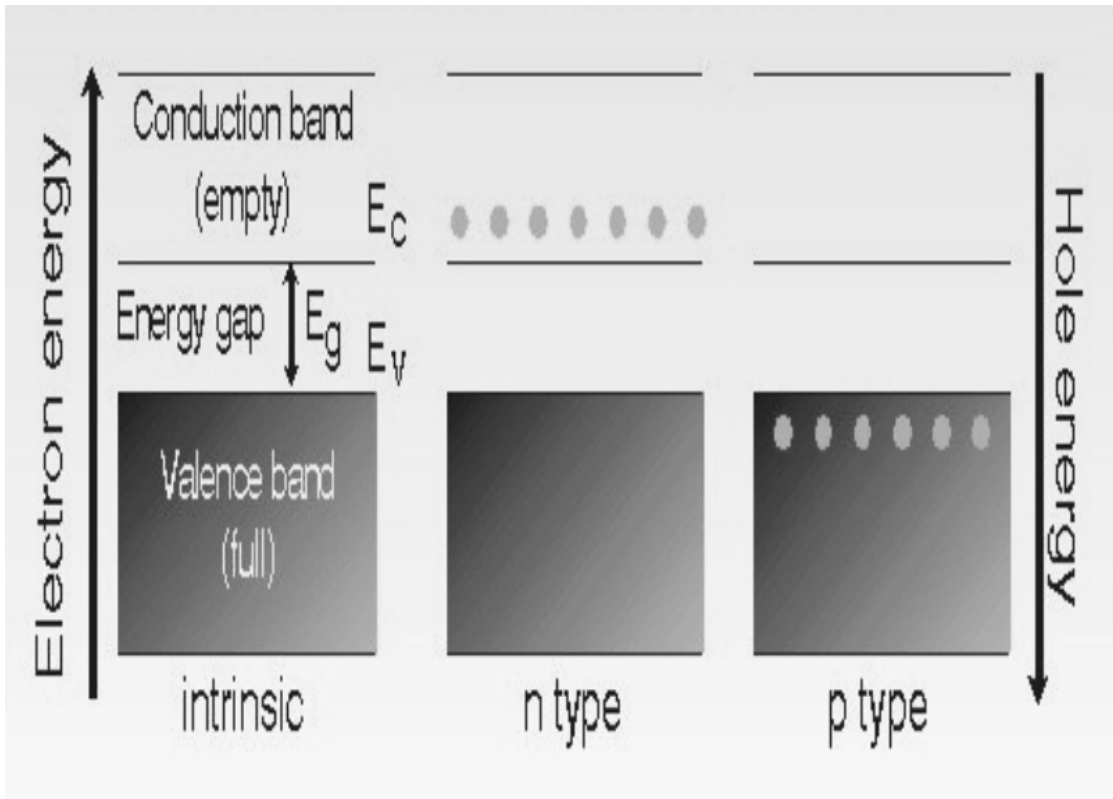


Fig. 1-2 Band diagram and the electron-hole distribution in semiconductors

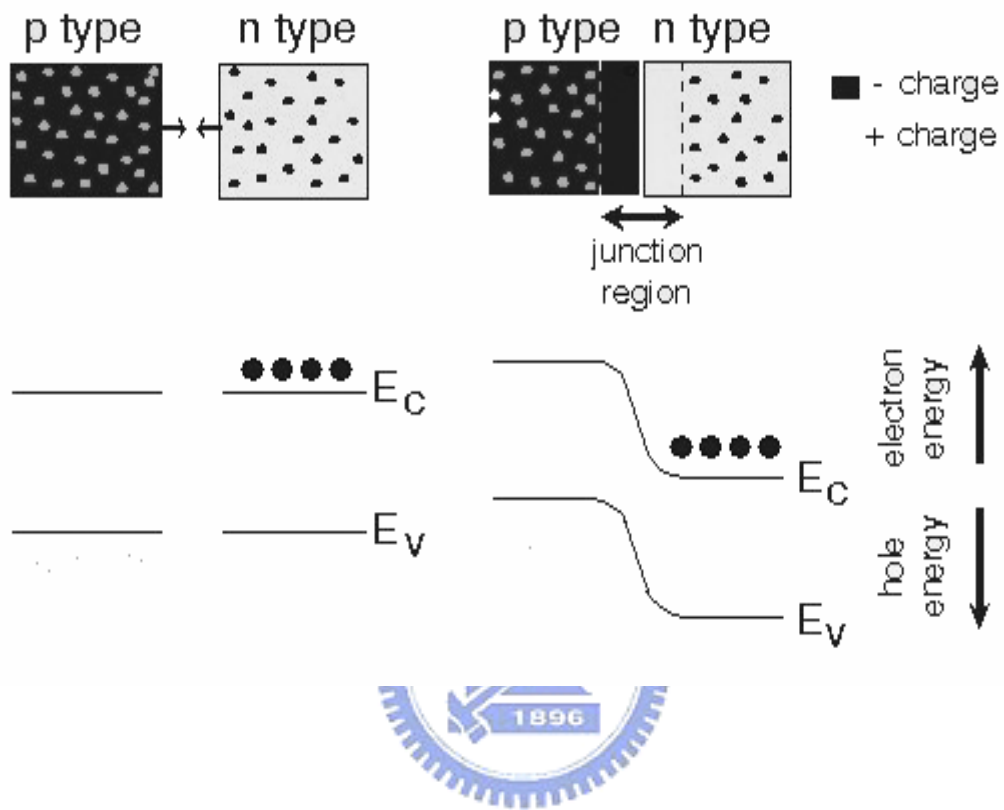


Fig. 1-3 Diagram of p-n junction formation and the resulting band structure

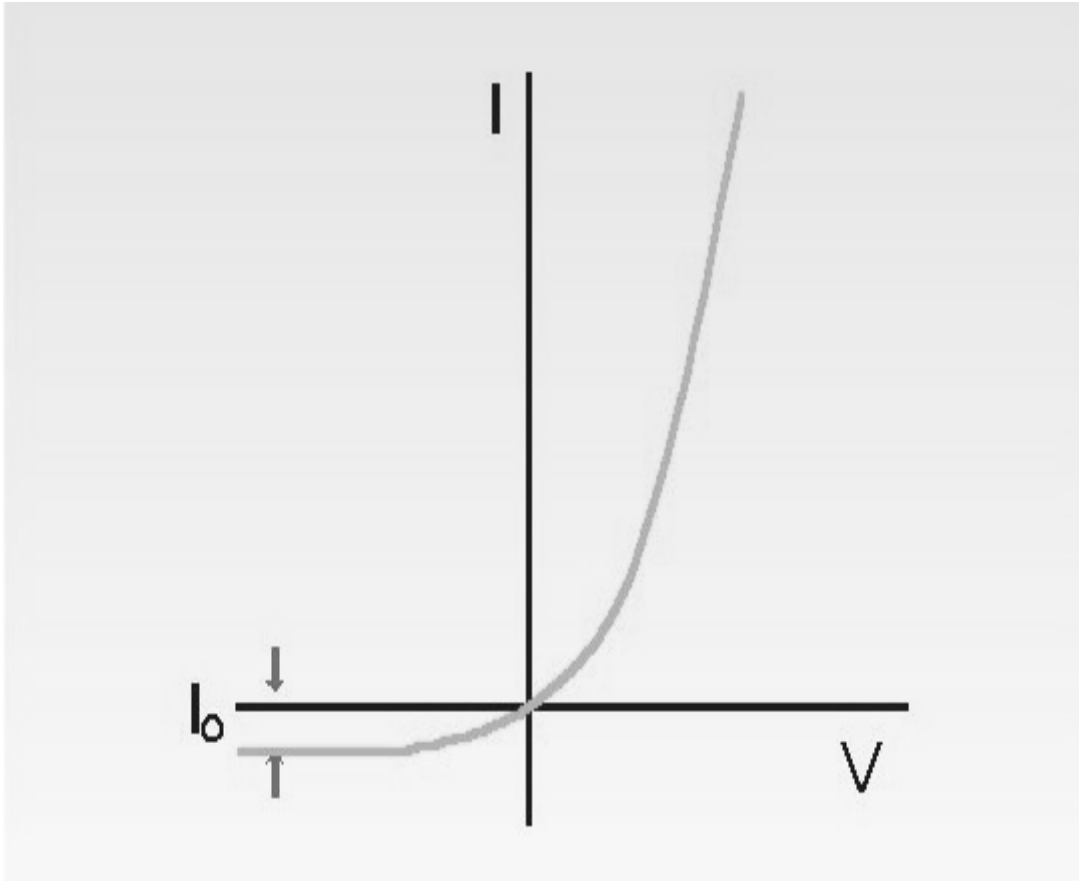


Fig. 1-4 The I-V characteristic of a diode

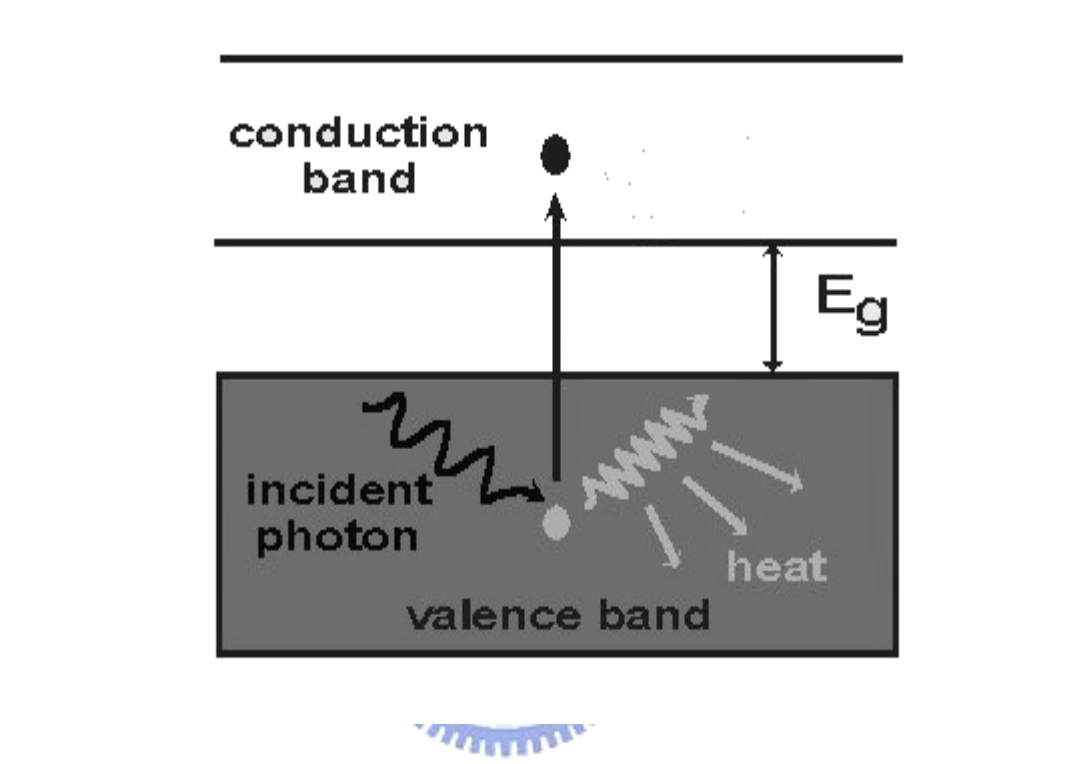


Fig. 1-5 The generation of electron-hole pairs by light

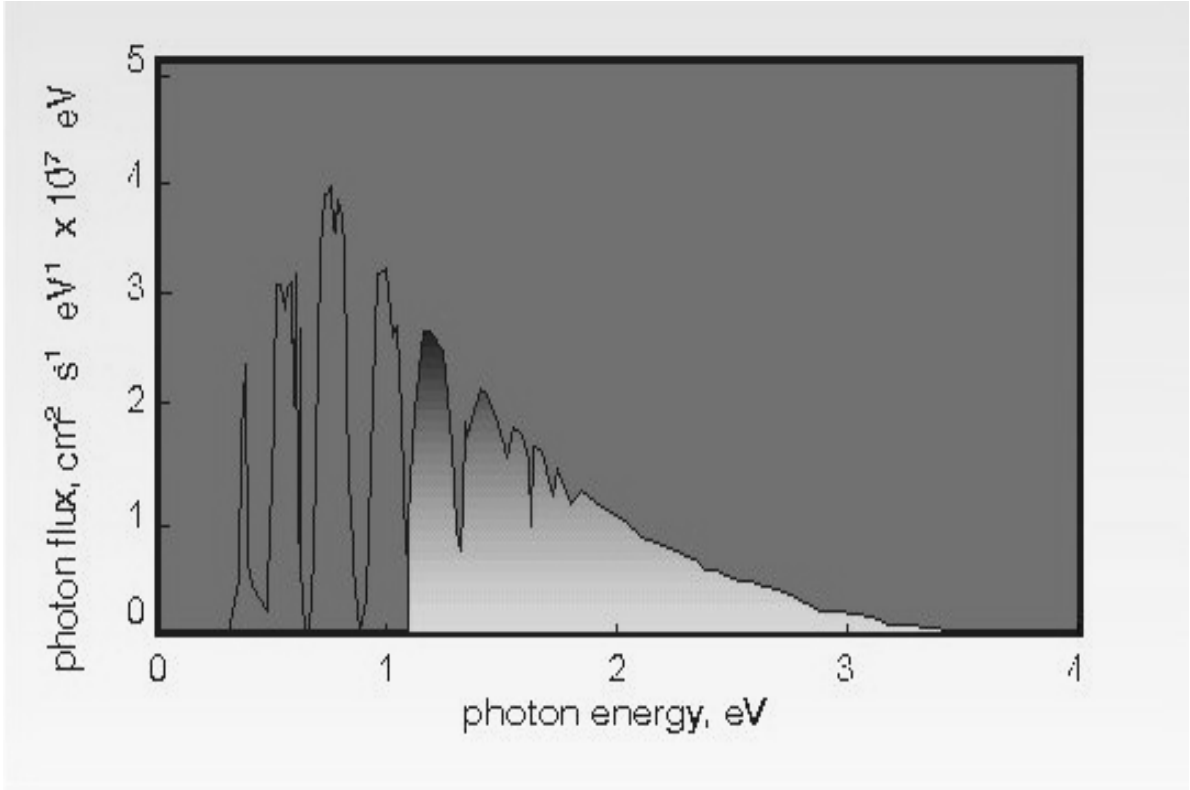


Fig. 1-6 Photon flux utilized by a silicon solar cell

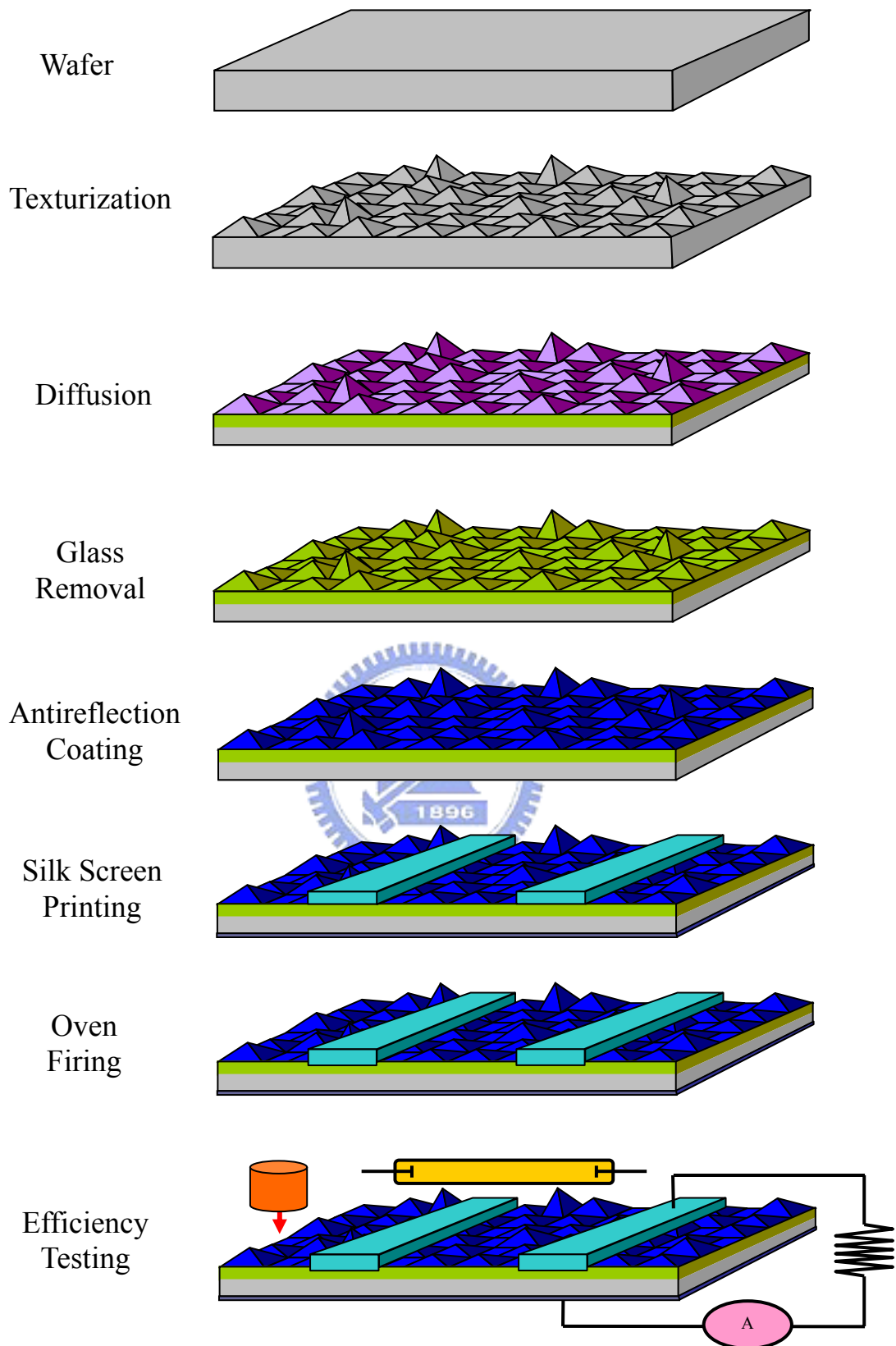


Fig. 1-7 The process of manufacturing silicon solar cells

Table 1-1 The bandgaps of the most important semiconductors for solar-cell applications

Material	Energy gap (eV)	Type of gap
crystalline Si	1.12	indirect
amorphous Si	1.75	direct
CuInSe ₂	1.05	direct
CdTe	1.45	direct
GaAs	1.42	direct
InP	1.34	direct

2. Mathematical and Physical Model

As mentioned, the molecular dynamics simulation is a well suited numerical method to calculate reflection caused by texturization of solar cells.

2.1 The Molecular Dynamics Method

The classical molecular dynamics scheme considers an n-atomic nonquantum system. Each atom i in this system is of its position r_i , velocity v_i and mass M . Thus the motion of a particle can be described as Newton's second law:

$$M \frac{d^2 r_i}{dt^2} = \sum_{j=1, j \neq i}^N F_{ij} \quad (2-1)$$

where F_{ij} is the force exerted by atom j on atom i . The force term is derived from the interatomic potential that must satisfy both nanoscopic and macroscopic requirements. The potential function generally forms with a short-distance repulsive term and a long-distance attractive term. Given initial conditions, Eq. (2-1) can be solved to provide the position and the velocity of each particle as a function of time, which will be used to compute the system temperature, heat flux, and thermal conductivity.

To avoid complications in photon-electron transformation, a rough and simple MD model was devised to govern this problem. In the classic mechanical MD simulations, a two-body attractive-repulsive potential model governs the interaction between two particles. For one particle, short-range repulsive forces rebound the too close particles from themselves, and long-range attraction catches other particles closer to itself in attractive force field. Assuming that the force field between an atom and photon is spherical, the 12-6

Lennard-Jones potential model with an undetermined parameter k , which is a short-range multiple, is adopted,

$$U(r) = 4 \left[k \left(\frac{1}{r} \right)^{12} - \left(\frac{1}{r} \right)^6 \right] \quad (2-2)$$

When photons reach the substrate with the non-dimensional light speed c^* and the impact angle θ , attraction and repulsion behaviors occur between silicon's atoms and photons. Figure 2-1 shows the mechanism of photon-atom interactions. When a photon enters the attractive field of an atom, the photon should be attracted to the center of atom. But the repulsive force pushes the photon off center if the photon is too close to the atom center.

The substrate is maintained as a NVE model (fixing particle numbers, system's volume and total energy) in the heat-transfer process, so the photons which enter the substrate are constrained because of forces among atoms and decay of motive energy of themselves. The system's temperature can be readily calculated from the velocity of each individual atom in the simulation domain since the Boltzmann distribution function allows the straightforward derivation of the mean kinetic energy $\langle E_c \rangle$ in the following way:

$$\langle E_c \rangle = \frac{1}{2} M \sum_{i=1}^N v^2 = \frac{3}{2} N k_B T_{MD} \quad (2-3)$$

where k_B is the Boltzmann constant and N is the number of particles in the system.

The initial temperature of the system was determined by Maxwell-Boltzmann distribution. During the indentation process, the velocity of every atom v^{new} was scaled as

$$v^{new} = v^* \sqrt{\frac{T_D}{T_A}} \quad (2-4)$$

where T_D is the desired temperature, T_A is the actual temperature, v^* is the calculated velocity of atom. In this paper, the temperature was set as 300K.

Due to the actions of attractive and repulsive forces and the photon's energy dissipation, the velocity of a photon which enters the substrate deeply tends toward zero. This behavior is considered photon absorption in a solar cell. However, some photons are repulsed at the substrate surface due to the repulsive force. This is considered reflection. The photons whose velocity decreases to zero were removed to avoid the increasing of particle numbers, and then affect the system's energy.

Note that the efficiency of mono-crystalline silicon is, at most, 24.7%, and the efficiency of GaAs crystalline PV cells is 25.7%[59]. This study attempts to make a model with an absorptance reaching to this theoretic value, 24.7% or 25.7% in a smooth, non-textured substrate by simply adjusting k . In our simulation, k is determined to be 3.86 in silicon and 4.2 in GaAs. After this calculation, simulations of varying surface texturization with this potential model can proceed. The smooth surface model is a reference, and the other texturing models in this paper, which are simulated with the same conditions, can then be compared with the reference model. This methodology not only reasonably avoids the complexity of photon-atom interaction but also achieves the goal of trying to evaluate the efficiency of two models with different surface texturization.

2.2 Predictor-Corrector Algorithms

Predictor-corrector methods are composed of three steps: prediction, evaluation, and correction. In particular, from the current position $x(t)$ and velocity $v(t)$ the steps are as follows:

1. Predict the position $x(t+\Delta t)$ and velocity $v(t+\Delta t)$ at the end of the next step.

2. Evaluate the forces at $t+\Delta t$ using the predicted position.
3. Correct the predictions using some combination of the predicted and previous values of position and velocity.

As a simple example, consider the following predictor-corrector based on Euler's method and applied to the one-dimensional harmonic oscillator (ODHO):

1. Predict $x(t+\Delta t)$ and $v(t+\Delta t)$ using Euler's method:

$$\begin{aligned} x(t+\Delta t) &= x(t) + v(t)\Delta t \\ v(t+\Delta t) &= v(t) + \omega^2 x(t)\Delta t \end{aligned} \tag{2-5}$$

2. Evaluate the force at $t+\Delta t$:

$$\frac{f(t+\Delta t)}{m} = \frac{dv}{dt} = -\omega^2 x(t+\Delta t) \tag{2-6}$$

3. Correct the predictions. Here we choose the same form as Euler's method but compute the slopes at the end of the step rather than at the beginning:

$$\begin{aligned} x(t+\Delta t) &= x(t) + v(t+\Delta t)\Delta t \\ v(t+\Delta t) &= v(t) - \omega^2 x(t+\Delta t)\Delta t \end{aligned} \tag{2-7}$$

The force evaluation implicit in (4.8) would actually be done in the previous step ($t-\Delta t$) and stored for use in the current step, so this algorithm meets the goals of requiring only one force evaluation per step while providing an algorithm of higher order than Euler's method.

Predictor-corrector methods offer great flexibility in that many choices are possible for both the prediction and correction steps. They may be either one-step, in which case they are

self-starting, or multistep methods, in which case something special must be done to start the calculation. With judicious combinations of predictor and corrector they offer good stability because the corrector step amounts to a feedback mechanism that can dampen instabilities that might be introduced by the predictor.

Any given predictor-corrector algorithm can be made more elaborate and of higher order by repeating the evaluation and correction steps. Let P be prediction, E be evaluation and c be correction. Then the procedure described above can be represented as PEC. If the corrected positions and velocities are used as second predictions, we obtain the algorithm $PEC(EC)=P(EC)^2$. Obviously, the E and C steps can be repeated as many times as desired, $P(EC)^n$. this strategy, while simple to implement, is rarely done in molecular dynamics because each e-step requires force calculations. A $P(EC)^n$ simulation will execute nearly n times slower than the PEC simulation.

Predictor-corrector algorithms were first introduced into molecular dynamics by Rahman[60]. Those commonly used in molecular dynamics are often taken from the collection of methods devised by Gear[61, 62].

Predict: molecular positions r_i at time $t+\Delta t$ using a fifth-order Taylor series based on positions and their derivatives at time t. thus, the derivatives \dot{r}_i , \ddot{r}_i , \dddot{r}_i , $r_i^{(iv)}$, and $r_i^{(v)}$ are needed at each step; these are also predicted at time $t + \Delta t$ by applying Taylor expansions at t:

$$r_i(t + \Delta t) = r_i(t) + \dot{r}_i(t)\Delta t + \ddot{r}_i(t)\frac{(\Delta t)^2}{2!} + \dddot{r}_i(t)\frac{(\Delta t)^3}{3!} + r_i^{(iv)}(t)\frac{(\Delta t)^4}{4!} + r_i^{(v)}(t)\frac{(\Delta t)^5}{5!} \quad (2-8)$$

$$\dot{r}_i(t + \Delta t) = \dot{r}_i(t) + \ddot{r}_i(t)\Delta t + \dddot{r}_i(t)\frac{(\Delta t)^2}{2!} + r_i^{(iv)}(t)\frac{(\Delta t)^3}{3!} + r_i^{(v)}(t)\frac{(\Delta t)^4}{4!} \quad (2-9)$$

$$\ddot{r}_i(t + \Delta t) = \ddot{r}_i(t) + \ddot{r}_i^{(iv)}(t)\Delta t + r_i^{(iv)}(t)\frac{(\Delta t)^2}{2!} + r_i^{(v)}(t)\frac{(\Delta t)^3}{3!} \quad (2-10)$$

$$\ddot{r}_i^{(iv)}(t + \Delta t) = \ddot{r}_i^{(iv)}(t) + r_i^{(iv)}(t)\Delta t + r_i^{(v)}(t)\frac{(\Delta t)^2}{2!} \quad (2-11)$$

$$r_i^{(iv)}(t + \Delta t) = r_i^{(iv)}(t) + r_i^{(v)}(t)\Delta t \quad (2-12)$$

$$r_i^{(v)}(t + \Delta t) = r_i^{(v)}(t) \quad (2-13)$$

Evaluate: the intermolecular force F_i on each molecule at time $t + \Delta t$ using the predicted positions. For continuous potential energy functions $u(r_{ij})$ that act between atoms i and j , the force on each molecule is given by

$$F_i = -\sum_{j \neq i} \frac{\partial u(r_{ij})}{\partial r_{ij}} \hat{r}_{ij} \quad (2-14)$$



Where \hat{r}_{ij} is the unit vector in the r_{ij} -direction. Evaluation of forces is time consuming because the sum in must be performed for each molecule i Newton's third law can be applied,

$$F(r_{ij}) = -F(r_{ij}) \quad (2-15)$$

to decrease the amount of computation by a factor of 2.

Correct: the predicted positions and their derivatives using the discrepancy $\Delta \ddot{r}_i$ between the predicted acceleration and that given by the evaluated force F_i . With the forces at $t + \Delta t$ obtained from eq.(2-14), Newton's second law eq.(2-1) can be used to determine the

accelerations $\ddot{r}_i(t + \Delta t)$. The difference between the predicted accelerations and evaluated accelerations is then formed,

$$\Delta\ddot{r}_i = [\ddot{r}_i(t + \Delta t) - \ddot{r}_i^P(t + \Delta t)] \quad (2-16)$$

In Gear's algorithms for second-order differential equations, this difference term is used to correct all predicted positions and their derivatives; thus,

$$r_i = r_i^P + \alpha_0 \Delta R2 \quad (2-17)$$

$$\dot{r}_i \Delta t = \dot{r}_i^P \Delta t + \alpha_1 \Delta R2 \quad (2-18)$$

$$\frac{\ddot{r}_i(\Delta t)^2}{2!} = \frac{\ddot{r}_i^P(\Delta t)^2}{2!} + \alpha_2 \Delta R2 \quad (2-19)$$

$$\frac{\dddot{r}_i(\Delta t)^3}{3!} = \frac{\dddot{r}_i^P(\Delta t)^3}{3!} + \alpha_3 \Delta R2 \quad (2-20)$$

$$\frac{r_i^{(iv)}(\Delta t)^4}{4!} = \frac{r_i^{(iv)P}(\Delta t)^4}{4!} + \alpha_4 \Delta R2 \quad (2-21)$$

$$\frac{r_i^{(v)}(\Delta t)^5}{5!} = \frac{r_i^{(v)P}(\Delta t)^5}{5!} + \alpha_5 \Delta R2 \quad (2-22)$$

Where

$$\Delta R2 \equiv \frac{\Delta\ddot{r}_i(\Delta t)^2}{2!} \quad (2-23)$$

The table shows the values of α_i parameters in Gear's Predictor-Corrector Algorithm for second-order differential equations using predictors of order q . The parameters α_i promotes numerical stability of the algorithm. The α_i depends on the order of the differential

equations to be solved and on the order of the Taylor series predictor. Gear determined their values by applying each algorithm to linear differential equations and analyzing the resulting stability matrices. For a q -order predictor, the values of the α_i were chosen to make the local truncation error of $O(\Delta t^{q+1})$; then the method will be stable for second-order differential equations with global truncation error of $O(\Delta t^{q+1-2})=O(\Delta t^{q-1})$.

2.3 Neighbor Lists

The most time-consuming part of a molecular dynamics simulation is calculation of the forces on the atoms. For a fluid of N atoms, the forces are computed by sampling, at each time step of the simulation, $1/2N(N-1)$ unique r_{ij} distances. But when a truncated potential is used, the force equals zero for any $r_{ij} > r_c$ (where r_c is the potential cutoff distance); consequently, evaluating distances r_{ij} that are greater than r_c wastes computer time.


This wasted time can be saved by using a bookkeeping scheme such as that originally devised by Verlet[63]. For each atom i , the method maintains a list of neighboring atoms that lie within a distance r_L of i ; so the list identifies those atoms that contribute to the force on atom i , the same neighbor list is used over several consecutive time steps, and it is updated periodically, say every 10 time steps. The list distance r_L is slightly larger than r_c so that j atoms can cross r_c and still be properly considered in evaluating the force on atom i . typically, $r_L = r_c + 0.3\sigma$.

For a three-dimensional Lennard-Jones fluid at density $\rho\sigma^3=0.8$. each atom has about 75 neighbors lying within a radius $r=2.8\sigma$ (which is the appropriate list distance when $r_c=2.5\sigma$). However, in the neighbor list for atom i , we need store only the identities of those neighbors j having $j>i$, because for $j<i$ atom i appears in the list as a neighbor of j . on average, about half the neighbors of i have $j>i$, so we need, for the neighbor list, about $75/2 \doteq 40$

storage locations per atom. Therefore to store the neighbor list in a simulation of 256 atoms, we use an array, call it LIST, containing about 11000 elements. We then use the elements of another array, NPOINT, to locate in LIST the neighbors of a particular atom. The relation between NPOINT and LIST is illustrated in Figure 2-5. by using two one-dimensional arrays rather than one two-dimensional array, we avoid the computational overhead involved in dealing with double subscripted variables. A neighbor list can provide substantial gains in execution speed, as shown in Table 2-4. To compare with the advantage of with and without list, a model of 140000 particles was also executed in our research and illustrated in Table 2-4.

The scheme just described is but one way by which a neighbor list can be implemented. It has the disadvantage that it does not vectorize to run on parallel machines; however, modifications can be made to overcome this handicap[64-67].

2.4 Model of Si and GaAs Solar Cells



Following this concept, mono-crystalline silicon was selected as the solar cell material. This is because silicon is the most common material in all types of solar cells, and its structure is simpler for using with a MD model. The results and conclusions of this study can also be extended to other solar cells, GaAs, InGaAs, InGaP, etc. The structure of mono-crystalline silicon is a fcc diamond structure, showed in figure 2-2(a), and GaAs crystalline substrate is arranged by zinc blende (zb) structure, showed in figure 2-2(b). According the reviews of previous studies, square, pyramidal and semicircular texturing were demonstrated. Figure 2-3 shows the physical models of the three samples in this paper. A single silicon cell has a diamond structure with 8 atoms. Under the texturing surface, three layers absorb the motion energy of photons. To avoid the effects of different lengths in the x - and y - direction, the substrate of solar cells is set as a square. Periodic boundary conditions are imposed in the x - and y -direction. Due to the periodic texturing shapes, different period lengths lead to different

numbers of atoms. In the case of different intervals of square texturization, at least six periods are chosen. So in the case of distance $d=1$ cell, the number of silicon atoms is 144352. The longer the distance, the more atoms are present in the substrate. The photon's incident angle varies at x - z plane.

With the same concept, a GaAs cell is also an *fcc* structure, with 4 Ga atoms and 8 As atoms. For more precise simulation, the interaction among Ga and As atoms is governed by 12-6 Lennard-Jones potential model and three-body Tersoff potential model[68, 69]. The Tersoff model is

$$E = \frac{1}{2} \sum_{j \neq i} f_c(r_{ij}) [V_R(r_{ij}) - b_{ij} V_A(r_{ij})] \quad (2-24)$$

The pairwise terms V_A and V_R are classical pairwise attractive and repulsive terms, whereas b_{ij} is a many body term that scales the attractive part to the repulsive one, the functional form of which will be given later. The pairwise terms are written as

$$V_R = \frac{D_e}{S-1} e^{-\beta\sqrt{2S}(r_{ij}-r_e)} \quad (2-25)$$

$$V_A = \frac{SD_e}{S-1} e^{-\beta\sqrt{27S}(r_{ij}-r_e)} \quad (2-26)$$

To restrict the calculation to just a certain number of nearest neighbors of the atom I under observation, a spherical cut off function f_c is introduced:

$$f_c(r) = \begin{cases} 1, & r_{ij} \leq D - D_{cut} \\ \frac{1}{2} \left[1 - \sin \left[\pi (r_{ij} - D) / 2D_{cut} \right] \right], & |r_{ij} - D| \leq D_{cut} \\ 0, & r_{ij} > D - D_{cut} \end{cases} \quad (2-27)$$

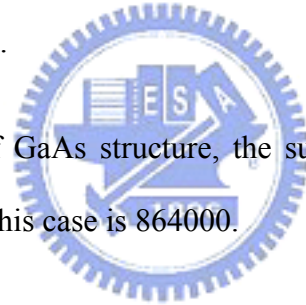
The system's temperature keeps at 300K. Table 1 shows the physical parameters of this model, and table 2 shows the parameters of Tersoff potential for GaAs.

The potential among photons is assumed as 0, as well as the potential among atoms of Si and GaAs solar cells. But in the GaAs case, the calculation of potential is to average the Lennard-Jones potential and Tersoff potential when a photon has interaction with atoms of substrate, so that the influence of structure difference can be enhanced. The interactive potential model between GaAs atoms and photons is adapted as

$$E = \frac{1}{2} (E_{LJ} + E_{Tersoff}) \quad (28)$$

Where the Lennard-Jones model is still determined by the reference skill mentioned above. The $k=4.2$ in GaAs case.

Due to the complex of GaAs structure, the substrate of GaAs is 120X120X5 cells. Thus the numbers of atoms in this case is 864000.



2.5 Amorphous Silicon

To form the amorphous SiO_2 , the method described by Vashishta *et al.*[70] was adopted, showed in Fig. 2-6. Due to avoid the effect of the initial state on the system, the amorphous state was obtained by heating crystal SiO_2 firstly and then equilibrating this material at a high temperature of 3000K and equilibrated for 60000 time steps. The system at 3000K was run for an additional 30000 time steps and the averages were evaluated over two segments of 15000n time steps each. Within statistical uncertainty, the averages over these two segments are found to be the same. The long simulations are necessary because the relaxation is much slower with the inclusion of three-body forces. The system at 3000K was cooled to 2500K and equilibrated for 30000 time steps. And again the averages were

calculated over an additional 15000 time steps. Using the same cooling schedule, a system at 2000K was obtained. In addition a system at 3500K was prepared by heating 3000-K system.

The molten state 2000K was quenched and thermalized at a rate of 0.1% per $10\Delta t$, leading to a state at 1500K. At this temperature, long-range diffusion ceases and the system undergoes thermal arrest. However, local rearrangements continue to take place because of considerable thermal energy in the system. This system was thermalized for 30000 time steps and then the averages were accumulated over an additional 30000 time steps. Using similar cooling and thermalization schedules, system at 300K were obtained. The system was set as NPT (isothermal-isobaric ensemble) model at the melted-quenched process because the volume changed when the structure was reformed. Then the system kept as NVE model at the heat-transported process.

2.6 Modified Model



From the previous studies [53, 54, 71, 72], we have interest about the phonon effect on the photovoltaic transform. At our previous study, we made an assumption that the atoms of substrate are fixed. But in the real situation, we know the phonon emission will be occurred and carried a part of heat out. So a part of energy will lose with thermal energy form. That is one of reasons that the efficiency of solar cells is limited. Thus we make a lot of simulations with phonon transport in the sequent studies.

The model with phonon transport is showed as Figure 2-7. When a photon collides with an atom, a part of photon's energy will be shared to the atom, causing the energy of atom to increase. So the vibration of atom increases. If the potential energy governs and connects the atoms in substrate, it seems a "spring" connects atoms. This vibration will transport through this spring structure.

Periodic boundary conditions are imposed in the x - and y -direction. In z -direction, when the photons collide with atoms, then the system is confined between two virtual “fixed” layers to avoid the effect of thermal expansion. Next the fixed layers on the top and bottom, the virtual atoms are assigned the lower temperature to form “cold” layers, which means a heat sink in this model. Heat flux in z -direction is developed due to temperature difference.

2.7 Flow Chat of Calculation

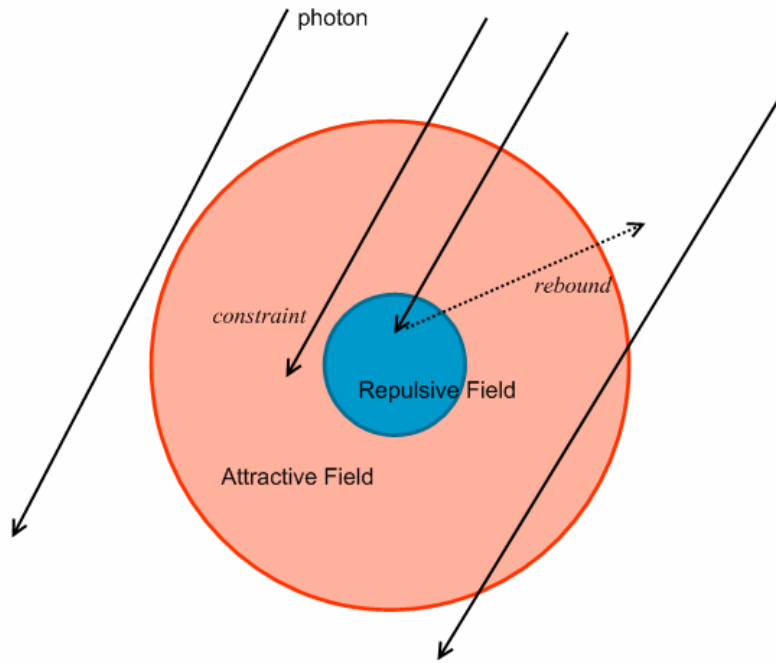
The flow chat of calculation in the research is illustrated in Figure 2-8. The calculation step is:

- (1). Set the initial value, including system temperature, numbers of particles in the system, the initial positions of all particles, boundary conditions and the condition for ending calculation etc.
- (2). To produce every particle's initial velocity by random generator. Repeat predicting the particle's position and velocity t the next step by using Gear's fifth-order Predictor-Corrector method to fit the condition that the particle's velocity distribution matches the classic Maxwell's velocity distribution.
- (3). To calculate the force of every particle by potential function. Then calculate the velocity, acceleration of every particle.
- (4). New position of every particle is determined.
- (5). Repeat step (3)-(4) until all the particles were calculated at the time step.
- (6). Display the movement of particles.
- (7). Repeat step (3)-(6) until the calculated time steps reach to what we initially set up.

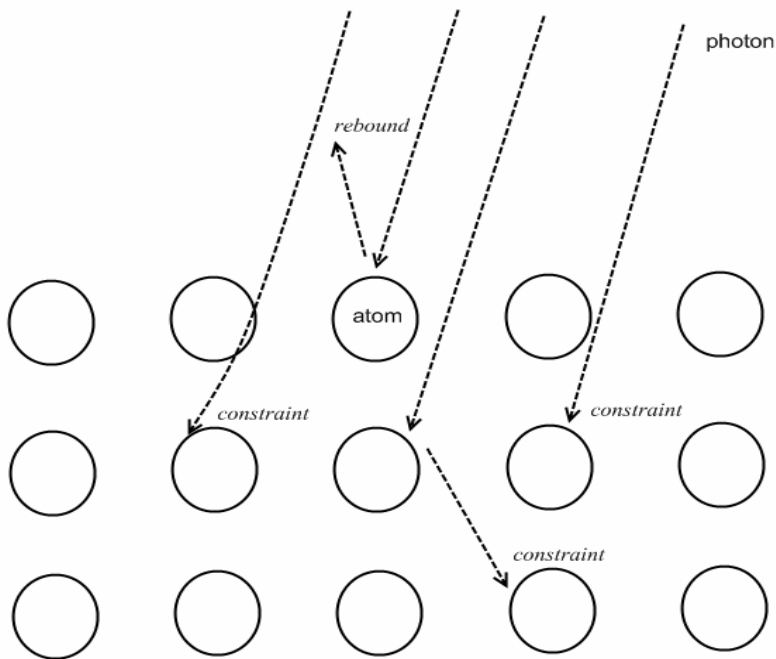
(8). Analyze and discuss the physical data from the execution of programs.

All the simulations were executed with the computer of AMD Athlon64X2 3800+ CPU, Fedora Core Linux 6 and the GNU project FORTRAN compiler g77.



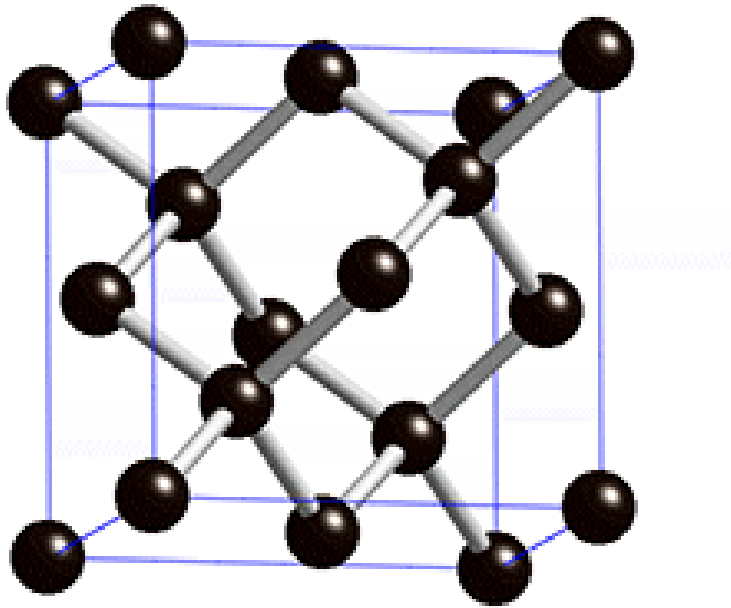


(a)

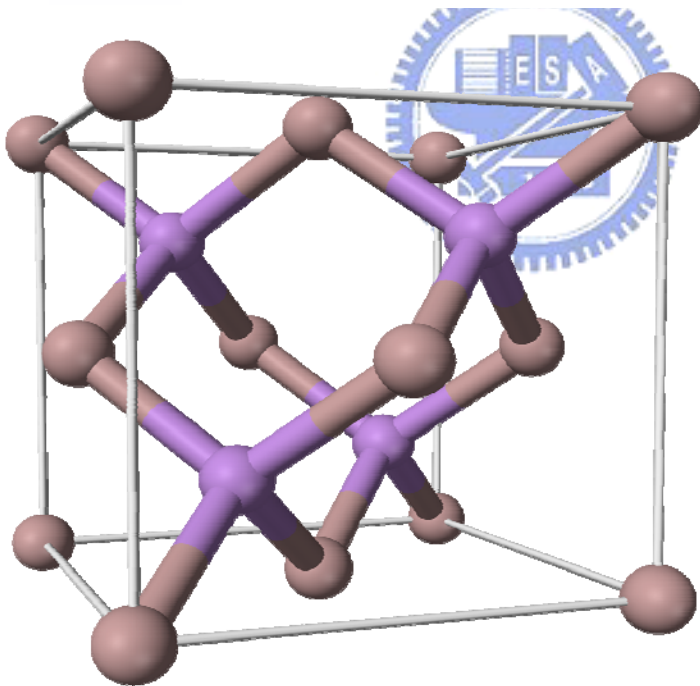


(b)

Fig 2-1 Illustrations of attractive and repulsive interaction of atoms and photons. (a) The photons moves toward repulsive force field are probably rebound out, and the other photons move through attractive field is constrained or decelerated. (b) The rebounded behavior is as same as reflection. The constraint behavior is as same as absorption.

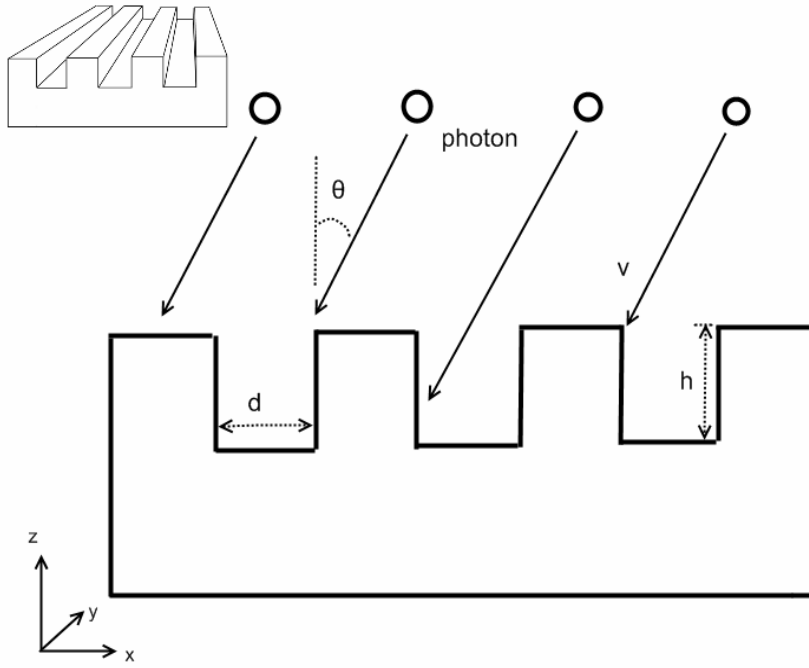


(a)

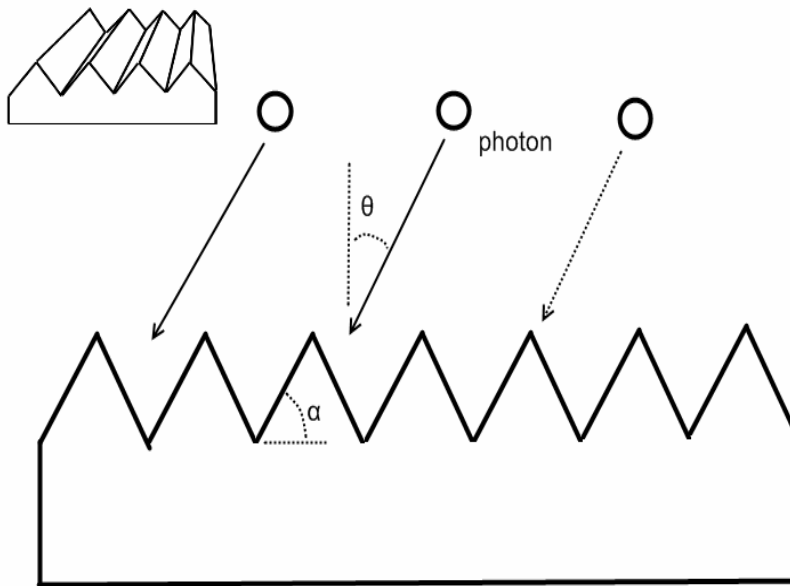


(b)

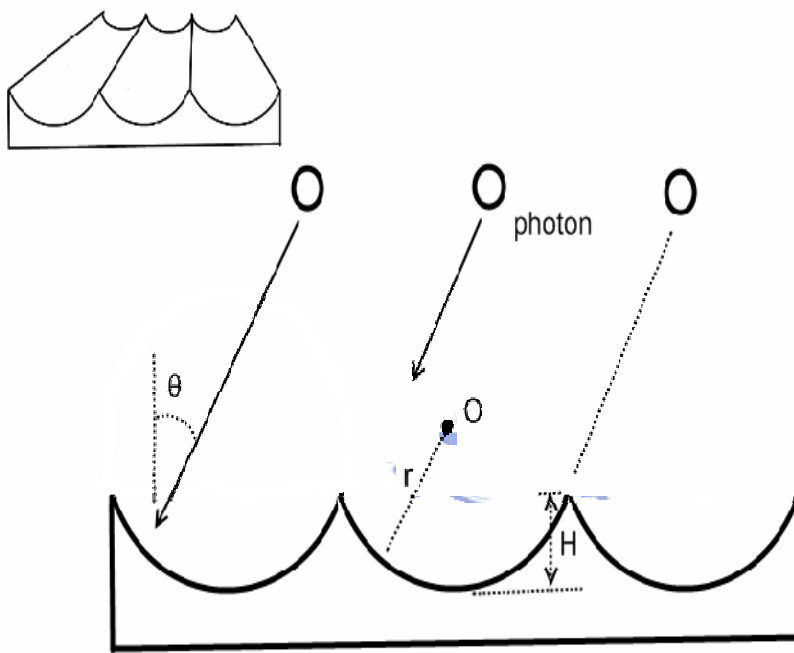
Fig. 2-2 The structure of (a) silicon, and (b) GaAs



(a)



(b)



(c)

Fig 2-3 Physical Model (a) square (b) pyramid (c) semicircle, the geometric variables are also shown in this figure

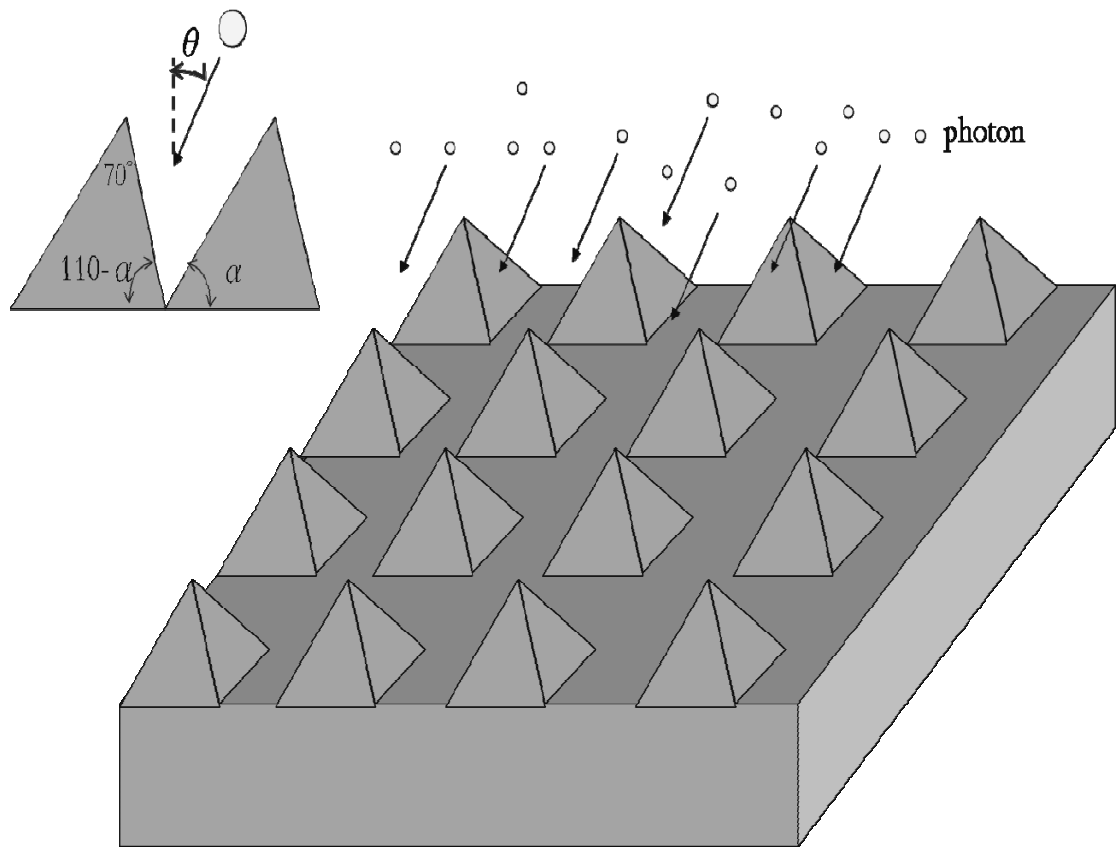


Fig. 2-4 The model of mc-silicon by alkaline etching. The tilted angle is α

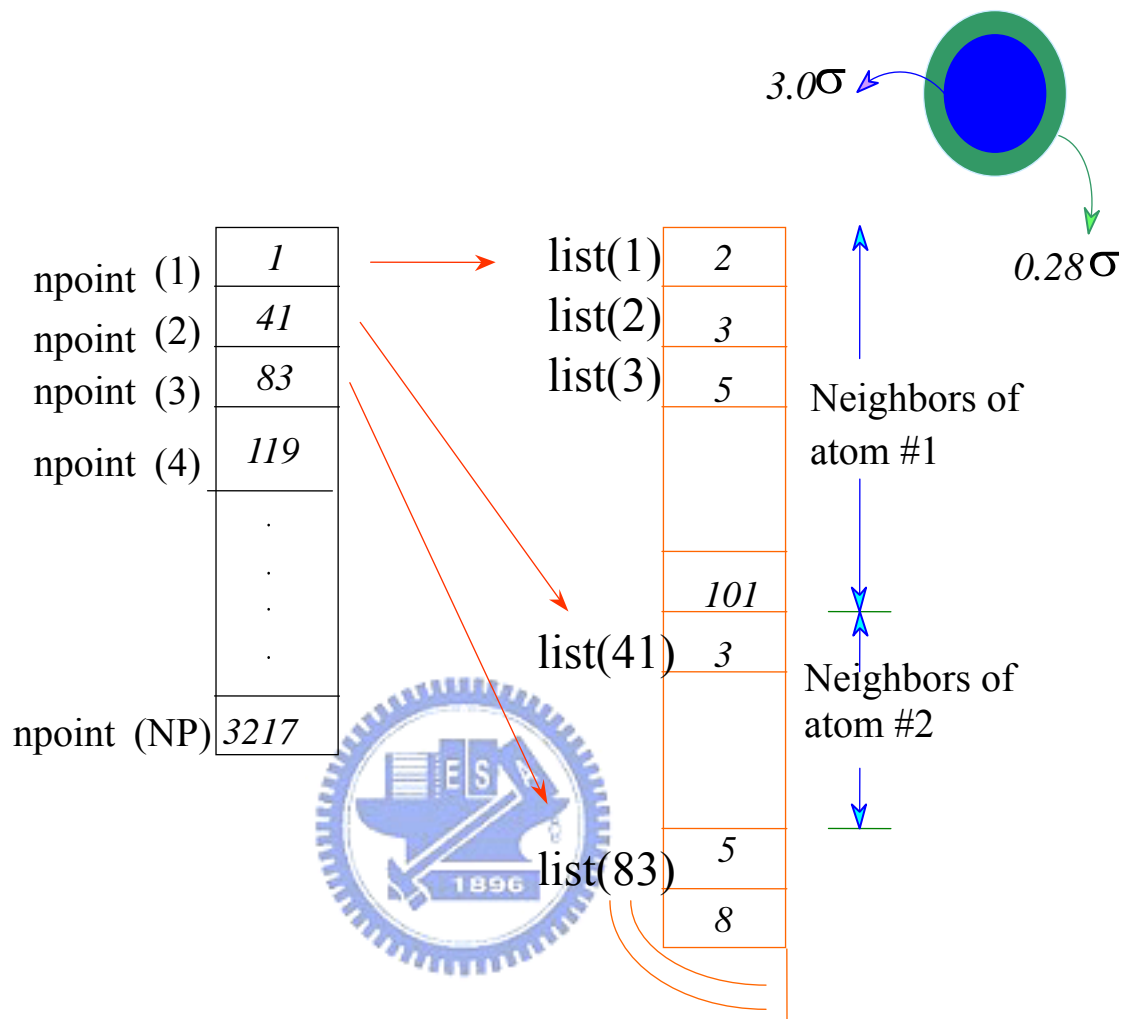


Fig. 2-5 Verlet List

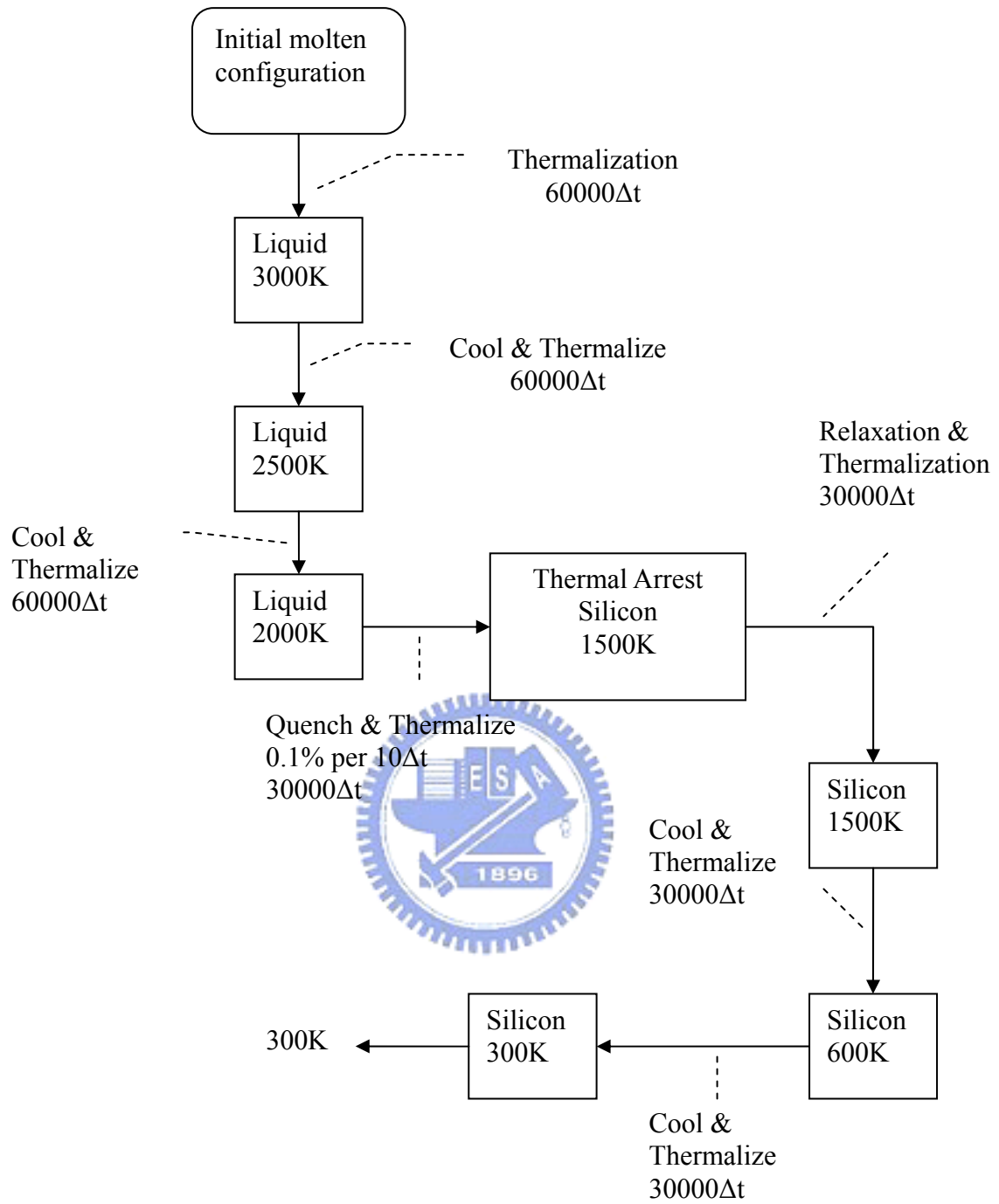


Fig. 2-6 The process to form amorphous substrate

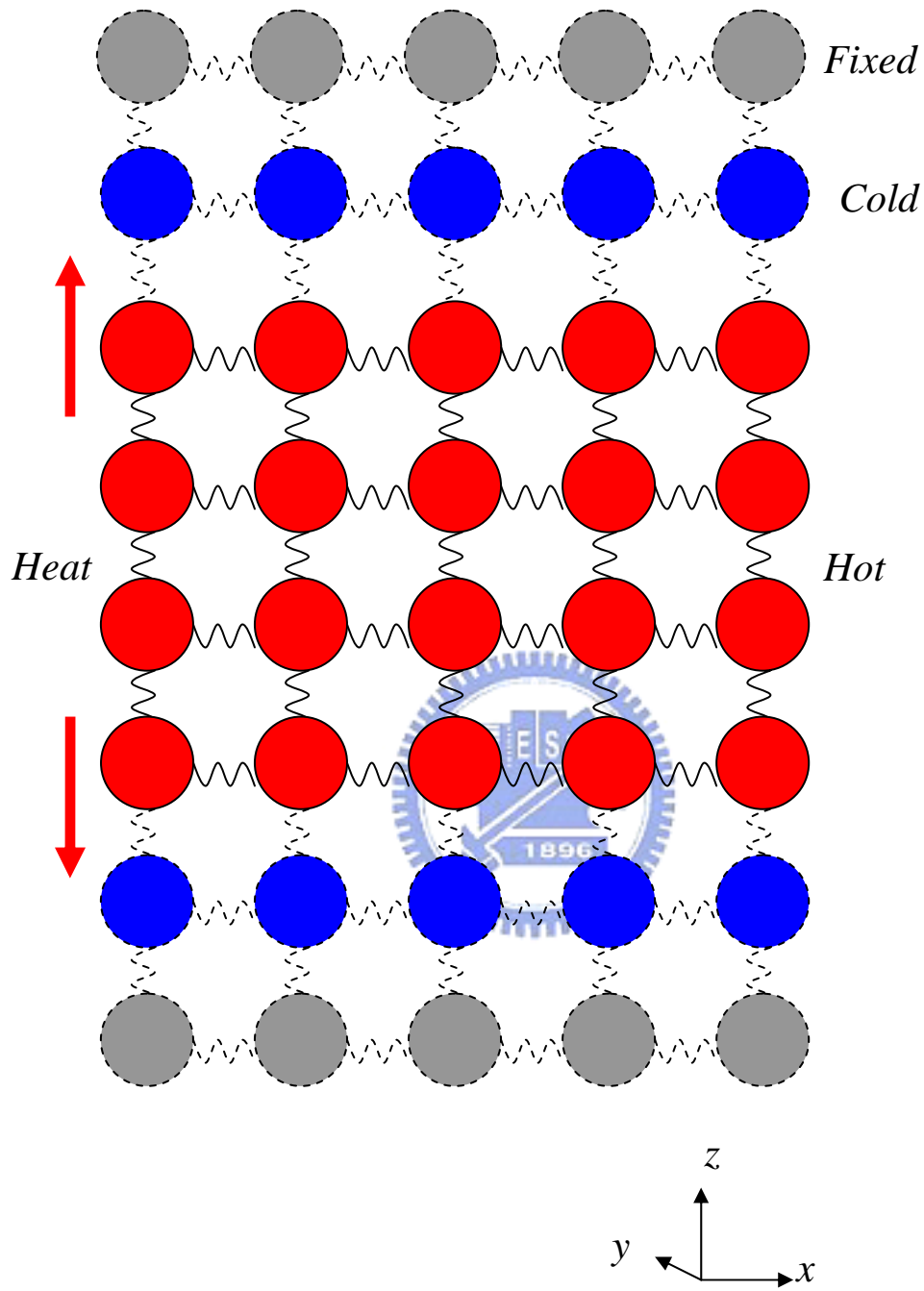


Fig 2-7 The model of phonon emission

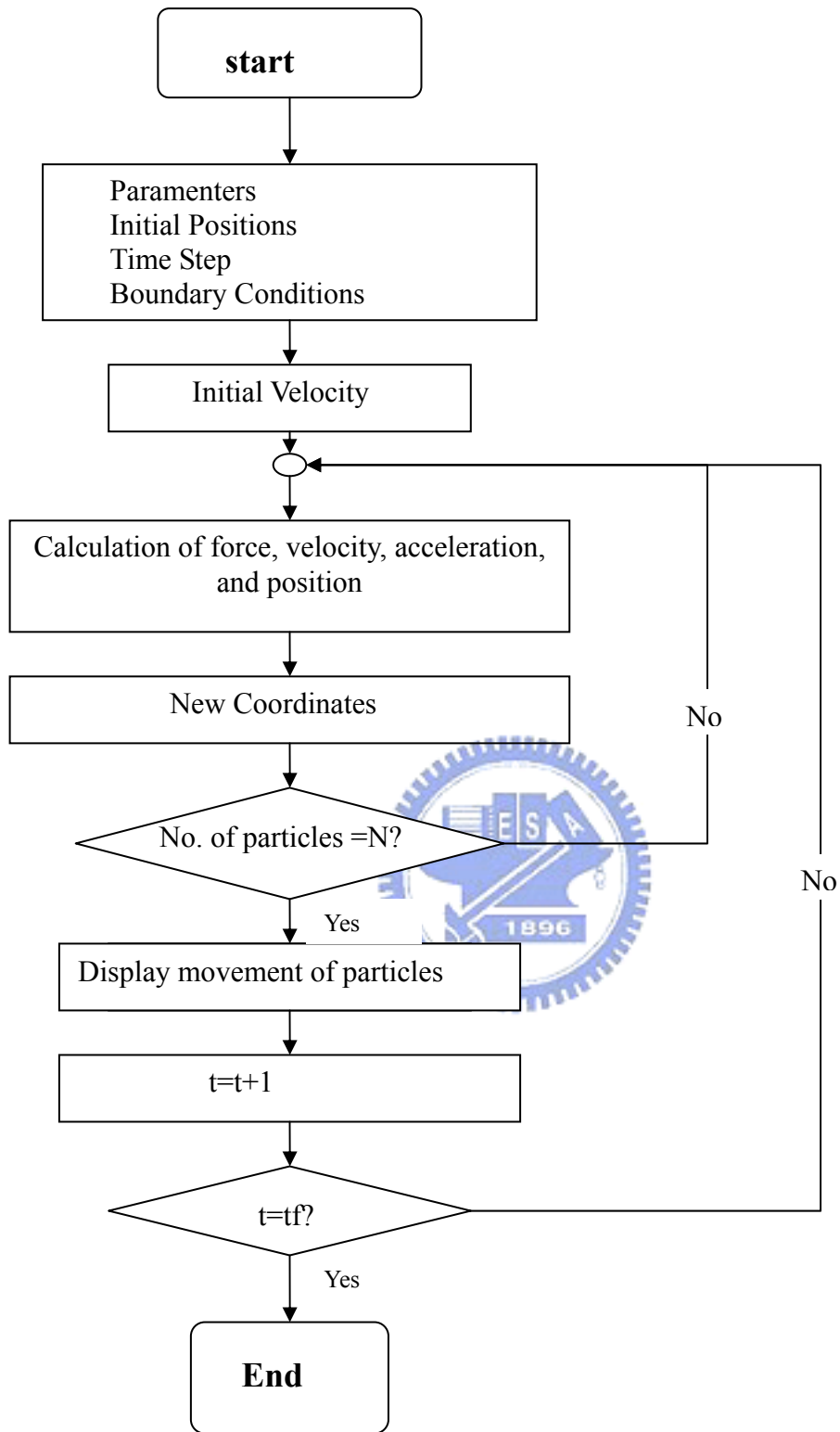


Fig 2-8 Flow Chart

Table 2-1 Parameters of physical models

<i>Fundamental Quantities</i>		
	silicon	GaAs
Mass (Density)	2.33 g/cm ³	5.32 g/cm ³
Length σ	5.431 Å	5.65 Å
Energy ϵ	1.792×10 ⁻¹⁹ J	1.424×10 ⁻¹⁹ J
Time t	1.77×10 ⁻³ ps/step	2.51×10 ⁻³ ps/step
<i>Normalized Quantities</i>		
Light speed (photon's speed) c*	4.8×10 ⁶	5.8×10 ⁶
Temperature T*	0.0231	0.033
Mass m*	0.54	0.54

Table 2-2 The parameters of Tersoff potential for GaAs

	Ga-As
D_e	1.78044
S	6.96025
λ	0.244341
γ	0.257183
β	1.5665
n	3.55586
c	2.16345
d	0.750147
$-h$	0.448899
Re	2.4324
D	3.5
D_{cut}	0.1

Table 2-3 Values of α_i parameters in Gear's Predictor-Corrector Algorithm for second-order differential equations using predictors of order q

α_i	$q=3$	$q=4$	$q=5$
α_0	1/6	19/120	3/16
α_1	5/6	3/4	251/360
α_2	1	1	1
α_3	1/3	1/2	11/18
α_4	—	1/12	1/6
α_5	—	—	1/60

Table 2-4 Speed of Execution of Lennard-Jones Program with and without Neighbor List

$\rho\sigma^3$	N	Average Number of Neighbors Stored per Atom	Relative Number of Time Steps Executed	
			No List	With List
0.6	108	27.2	6.7	9.7
	256	27.5	1	3.3
0.8	108	28.0	5.3	8.1
	256	38.1	1	2.6
0.8 (My research)	140000	72.2	1	7.6

3. Results and Discussion

3.1 Mono-crystalline Si solar cells

First of all, we consider the 2-dimensional model of Si solar cells. Figure 3-1 shows the relationship between the height of square texturing and absorptance for the square surface case. When $h=0$, the surface of solar cells is smooth, and the absorptance is 0.247 at an incident angle of 0 degrees. When surface texturing exists, the specimen with a greater square height has higher absorptance. However, the rate of increase becomes smaller as the height increases. Photons can easily drop into the holes with higher walls, so the substrate absorbs more photons. If the incident angle of photons increases, the absorptance lessens because more photons rebound.

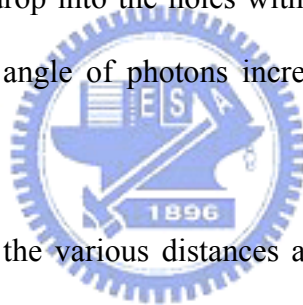


Figure 3-2 shows how the various distances affect the absorptance. As the distance increases, the absorptance obviously decreases when the square height is 2.31\AA . As in Fig. 3-3, the absorptance decreases as the incident angle of the photons increases. The absorptance decreases slowly when the distance surpasses 6.94\AA . In other words, the effect decreases as the distance increases.

The next example simulates a pyramidal surface. Figure 3-3 shows the influence of the facet tilt angle α . In this figure, the absorptance increases as the tilt angle α increases. Moreover, the rate rises quickly when α is more than 30 degrees. This result indicates that a more acute pyramid structure causes a decrease in reflection. Hylton *et al.* [16] discussed the possible path of light incident upon geometrically textured surface in air and concluded that a blunter facet tilted angle (sharp pyramid) facilitates light double-bounce incidence, thereby

reducing surface reflection. Our results agree with that conclusion. However, the current results are totally contrary to the research by Xi *et al.*[15]. This is because the present study assumes the pyramid to be isosceles; thus, the pyramids become sharper and taller with increasing α . This supposition leads to this phenomenon. As expected, a larger incident angle causes lower absorptance. Figure 5 shows this result.

Finally, Fig. 3-4 shows the case of a semicircular surface. Varying the ratio of H/r , the absorptance shows a clear rising trend from 0.247 at $H/r=0$, at which the surface of substrate is smooth, to a semicircular hole, $H/r=1$, if vertical light meets the substrate. Obviously, the increasing rate of absorptance decreases if H/r rises. The same trend occurs at 30, 45 and 60 degrees of the incident angle, but the magnitude of absorptance is lower than that exposed by vertical light. This trend of absorption agrees well with the findings of Xi *et al.*[15]

3.2 Multi-crystalline (mc) Si solar cells

This case is to discuss the variety of light absorptance of multi-crystalline Si substrate etched by alkaline solutions, shown in figure 3-5. According the discussion by Xi *et al.* [1], the tilted pyramids usually forms on the surface of mc-Si substrate etching by alkaline solution. If the orientation of the grains tends to (100), the pyramid will form a triangle with 70° on the top, tilted angle α and $110^\circ-\alpha$ on the other angles. So we try to make simulation with this model, and the results can easily compare with the results of Xi *et al.* [1].

Figure 3-6 shows the reflection hardly changes when the tilted angle is less than 20° . That is because the most light reflects from O_1 plane to O_2 plane in figure 3-5. More second reflection means more light will be absorbed by the substrate. But if the tilted angle surpasses 20° , the reflectance increases quickly. Therefore, the pyramids with a large tilted angle lead to the lower efficiency. To compare with the results of Xi *et al* [1], these two results are with a

good agreement.

Furthermore, we try to change the incident angle θ , shown in figure 3-7. In the case of pyramid with tilted angle $\alpha=30^\circ$ (the three angles are 70° , 80° and 30°), more second reflection produce when the incident angle $\theta=20^\circ\sim 85^\circ$, so the absorptance rises higher to almost 60%. But once the incident angle is greater than 80° , the possibility of second reflection decreased because the incident light is perpendicular to plane O_2 . Thus the absorptance quickly decreased. As the similar situation, when the incident angle is smaller than -20° , the incident light is also perpendicular to plane O_1 , the possibility of second reflection decreased, so the absorptance decreased to almost 20%.

We are interested about the effect of azimuth angle of incident light with absorptance. The surface morphology of the alkaline-etched wafers is quantified using a spherical polar coordinate system, as was the case for describing the relationship between different wafer and crystal orientations, shown in figure 3-8. However, in this case, the tilt (α) and azimuth (φ) angles refer to the positions of the normals to a particular facet of textured surface exposed by etch. These angles are measured relative to a particular crystal or wafer orientation, whose surface is parallel to the XY plane in the coordinate system and whose surface normal is parallel to the Z axis. The positions of the etch facets formed on a particular crystal or wafer orientation are thus described in terms of their angles α and φ with respect to the base orientation.

The simulation is proceeding with the conditions of the incident angle $\theta=30^\circ$, isosceles pyramid of tilted angle $\alpha=55^\circ$, and the azimuth angle $\varphi=0^\circ$ to 90° , to explore the influence of azimuth angle to the absorptance of solar cells with pyramid surface. In figure 3-9, it is found that the absorptance is greatest when the azimuth angle $\varphi=0^\circ$ or 90° , the incident light is perpendicular to the (100) plane for the azimuth angle. The reflective light is usually reflected

by planes of another pyramid. The higher probability of second reflection leads to the higher absorptance. But when the azimuth angle is getting larger, more incidents reflect only once, the probability of second reflection slightly decreased. Thus the absorptance also decreased. When the azimuth angle is greater than 45° , the incident light illuminate the (010) plane. The absorptance slightly increases again.

3.3 GaAs Solar Cells

We proceeded to make the simulations with similar square texturization case in mono-crystalline silicon, section 3.1. In the case of square surface, the relations between height of square texturing and absorptance were demonstrated in fig 2-3(a). Figure 3-10 shows the absorptance is 0.257 in incident angle of 0 degree when $h=0$, that means the surface of solar cells is smooth. When surface texturing exists, it can be found the specimen with more height of squares has higher absorptance. But the increasing range goes lower with height increasing. It's reasonable that photons easily drop into the holes with higher walls, so more photons are absorbed by substrate. If the incident angle of photons increases, it is noted that the absorptance lessens because more photons are rebounded.

Fig 3-11 shows how the various distances effect on the absorptance. When distance increases, the absorptance obviously decreases under the square height is 5.653\AA . The absorptance decreases with the increasing of incident angle of photons. It is regarded that the absorptance decreases slowly when the distance surpasses 16.959\AA . That means the effect reduces when the distance is longer enough.

We also applied this model with same LJ potential to the amorphous substrate. An amorphous substrate was made by the melting method in section 2-5. And the simulation of the relationship between the height of square texturing and absorptance for the square surface case similar with section 2-1 was made. Figure 3-12 showed the values of amorphous

substrate were lower than those of crystalline substrate. The absorptance of plate amorphous substrate decreased to 22.3%. The phenomenon of increasing of the amount of reflective photons was observed. The possible reason was the distance among atoms is closer than that among crystal structure. The closer distance caused less photon impacted into the substrate and more photons were reflected.



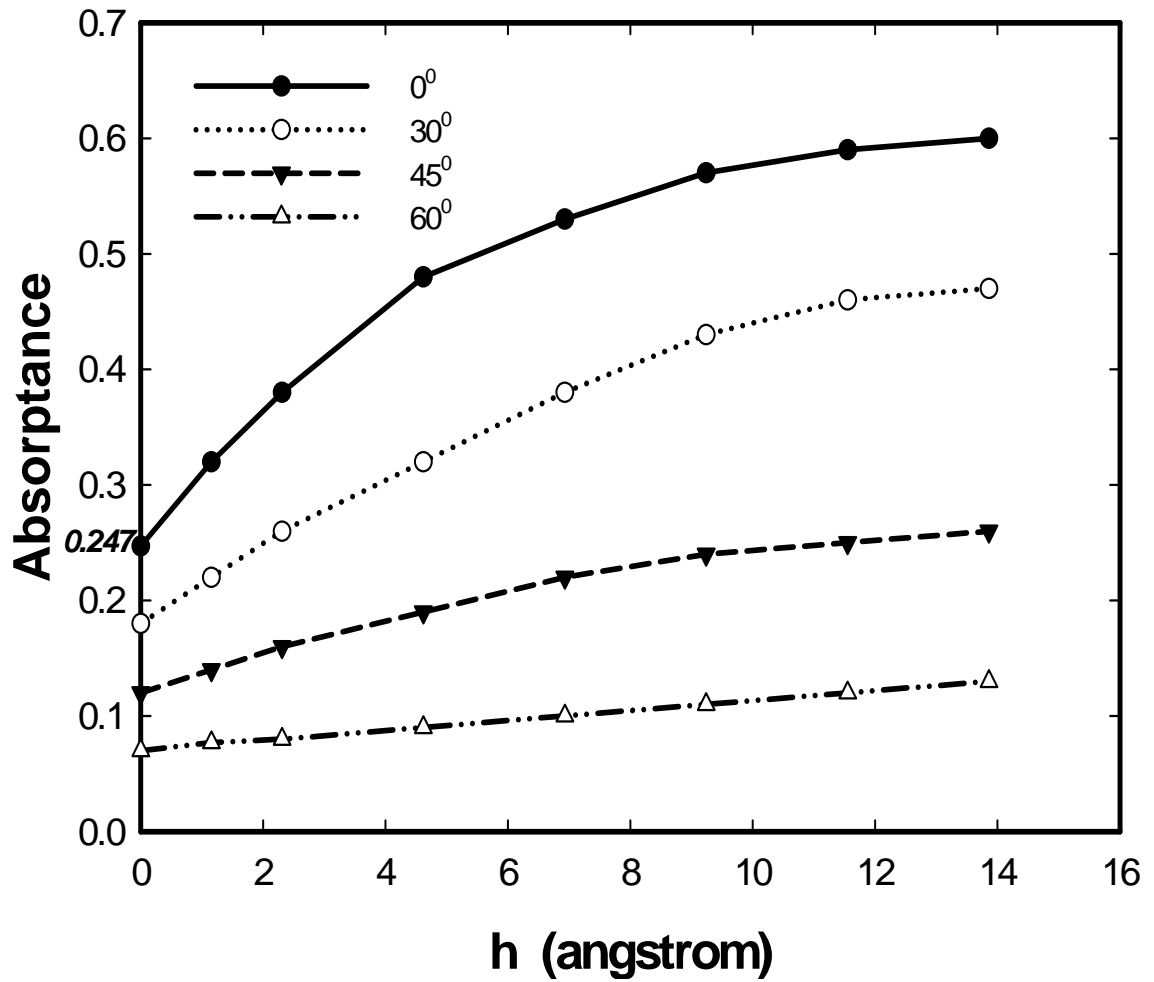


Fig 3-1 The relation among absorbance, h and photon's incidence angle θ of mono-crystalline silicon

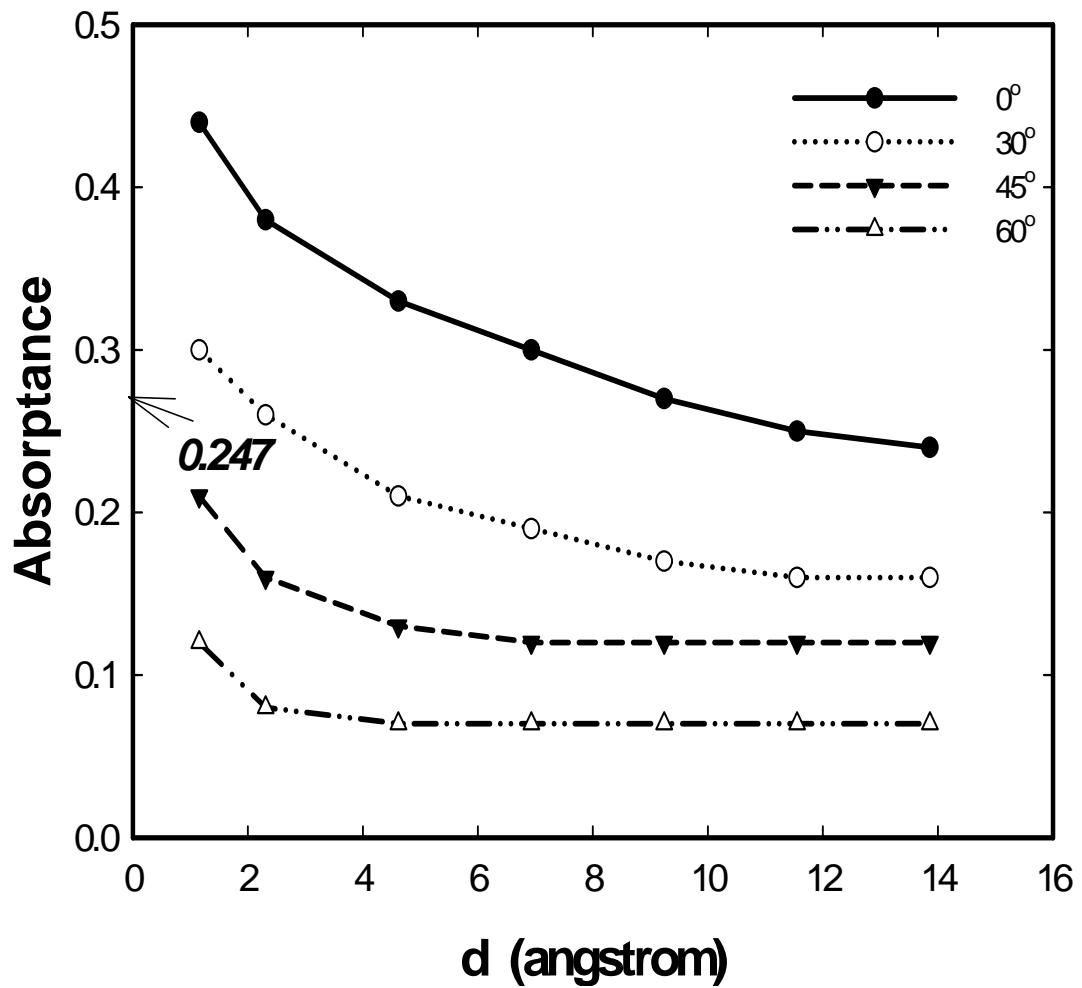


Fig 3-2 The relation among absorptance, distance and photon's incidence angle θ of mono-crystalline silicon

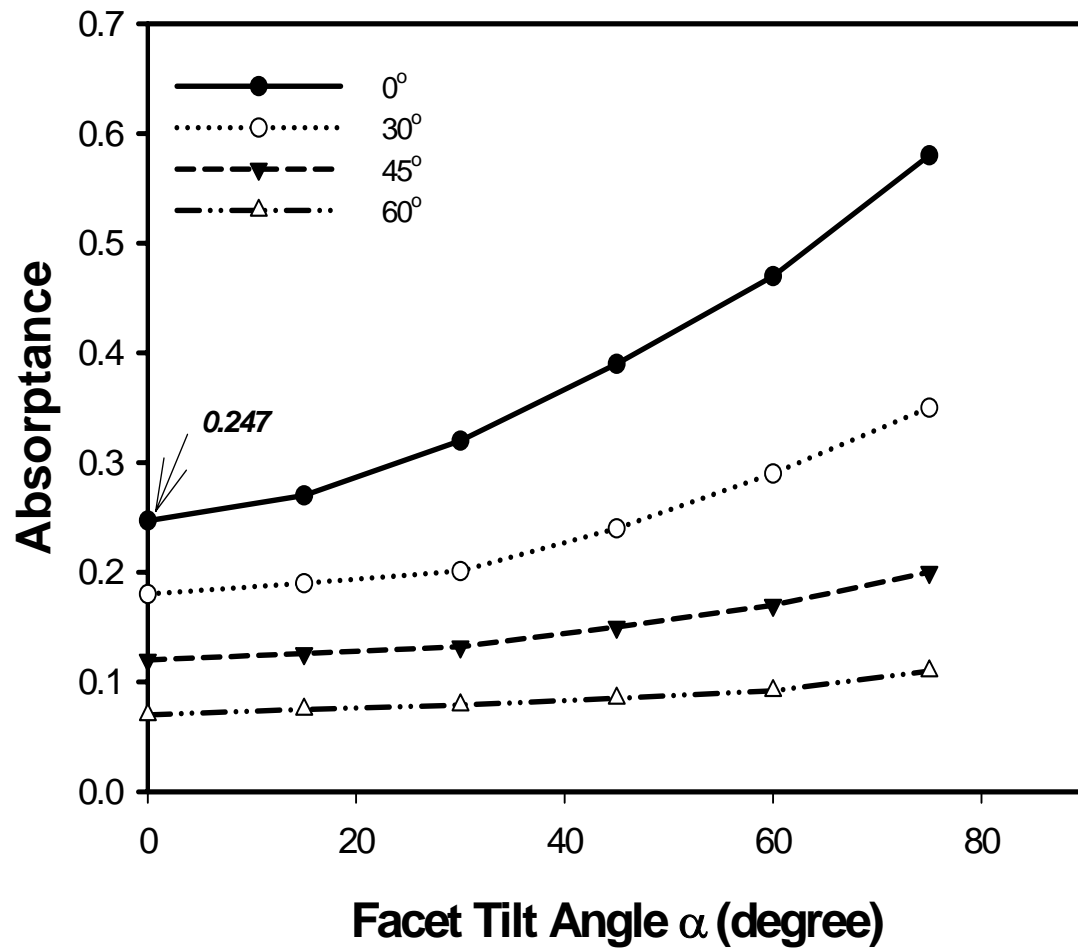


Fig 3-3 The relation among absorptance, facet titled angle α and photon' incidence angle θ of mono-crystalline silicon

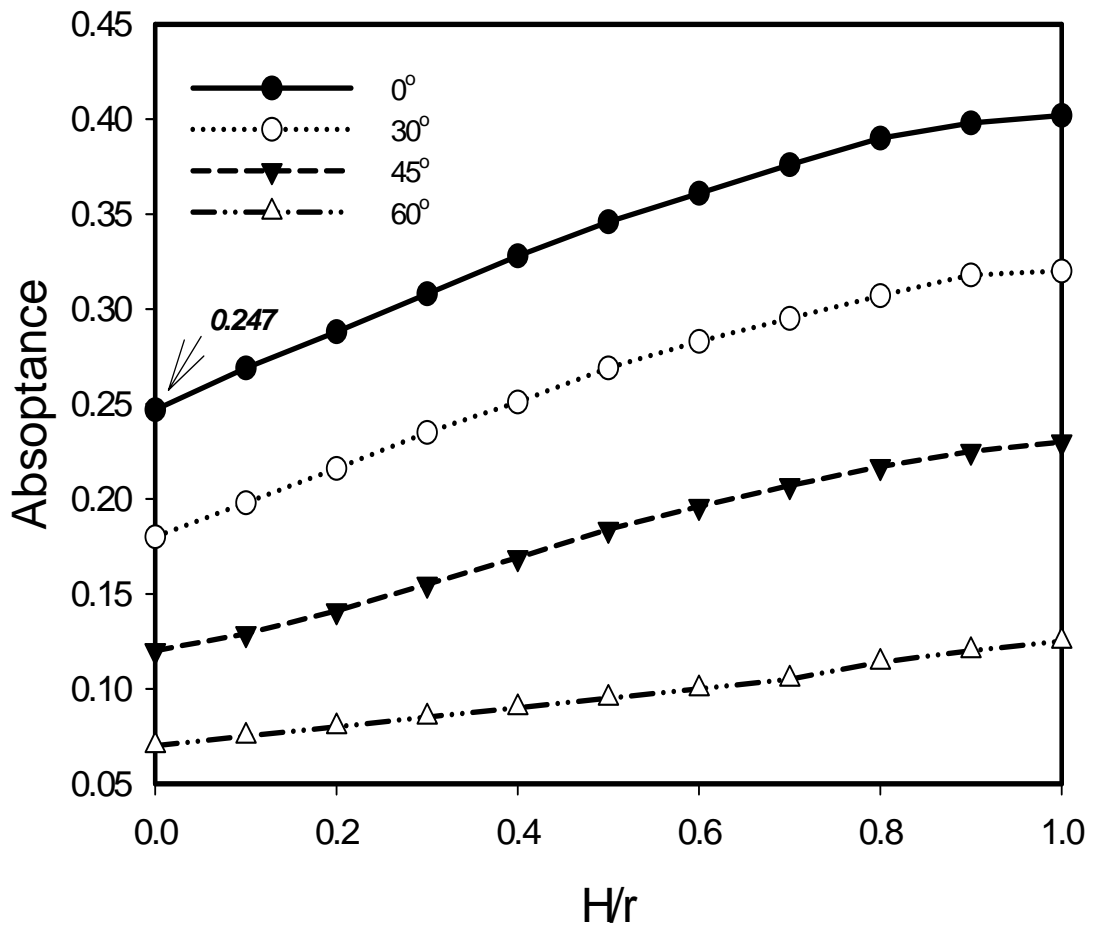


Fig 3-4 The dependence of absorptance on H/r in the case of semicircular texturing surface of mono-crystalline silicon.

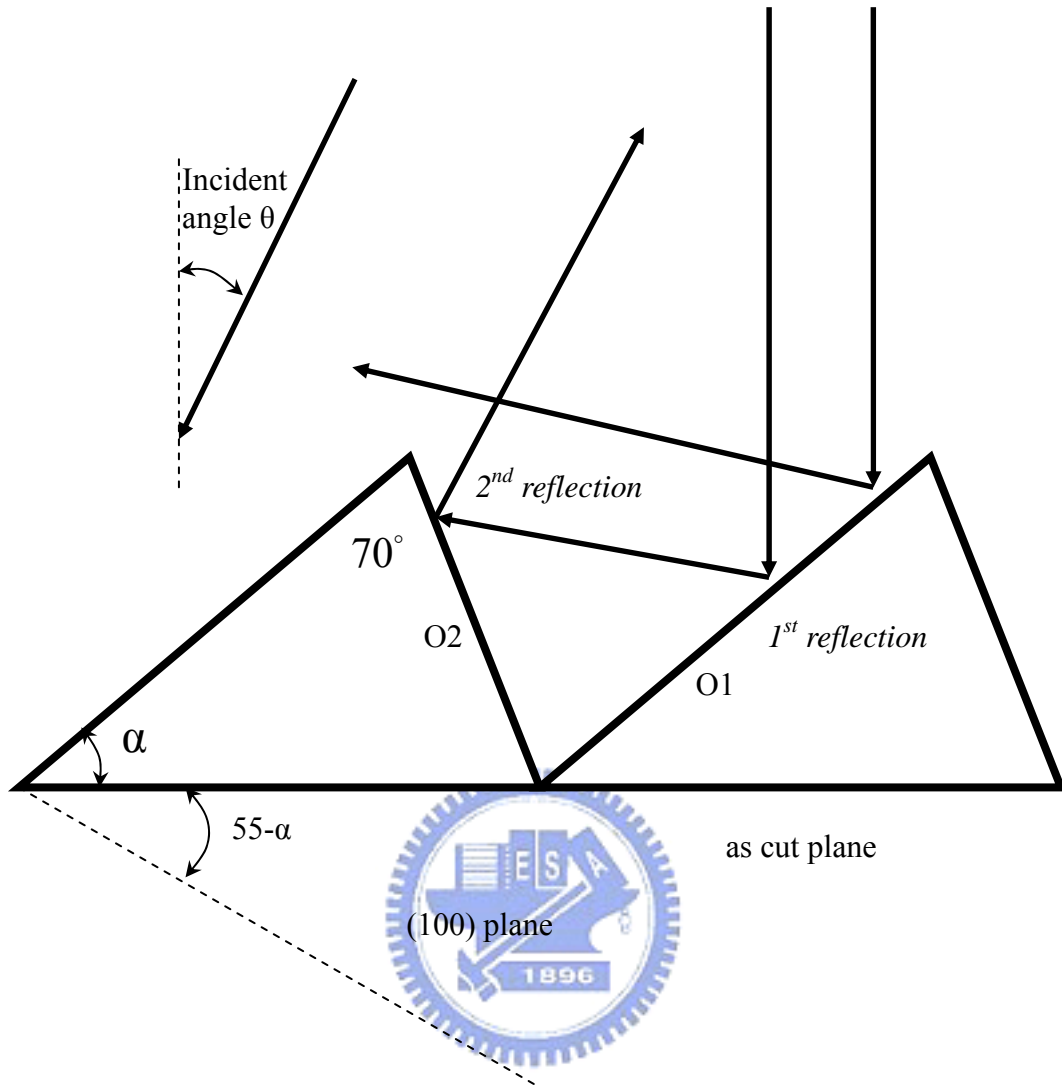


Fig. 3-5 Schematic illustration of reflection on the surface of mc-silicon after alkaline etching

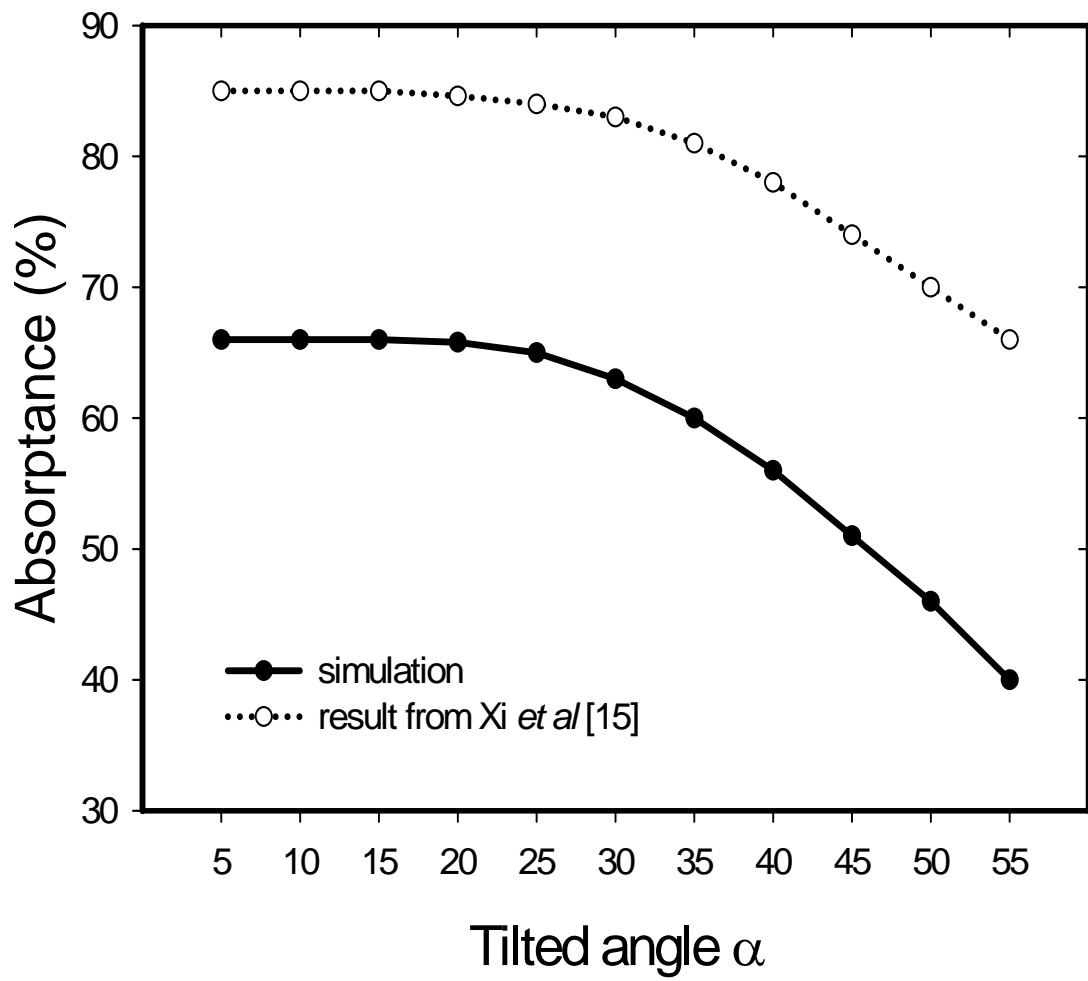


Fig. 3-6 The relation of absorptance and the tilted angle, agreeing with the result of Xi *et al.*[1]

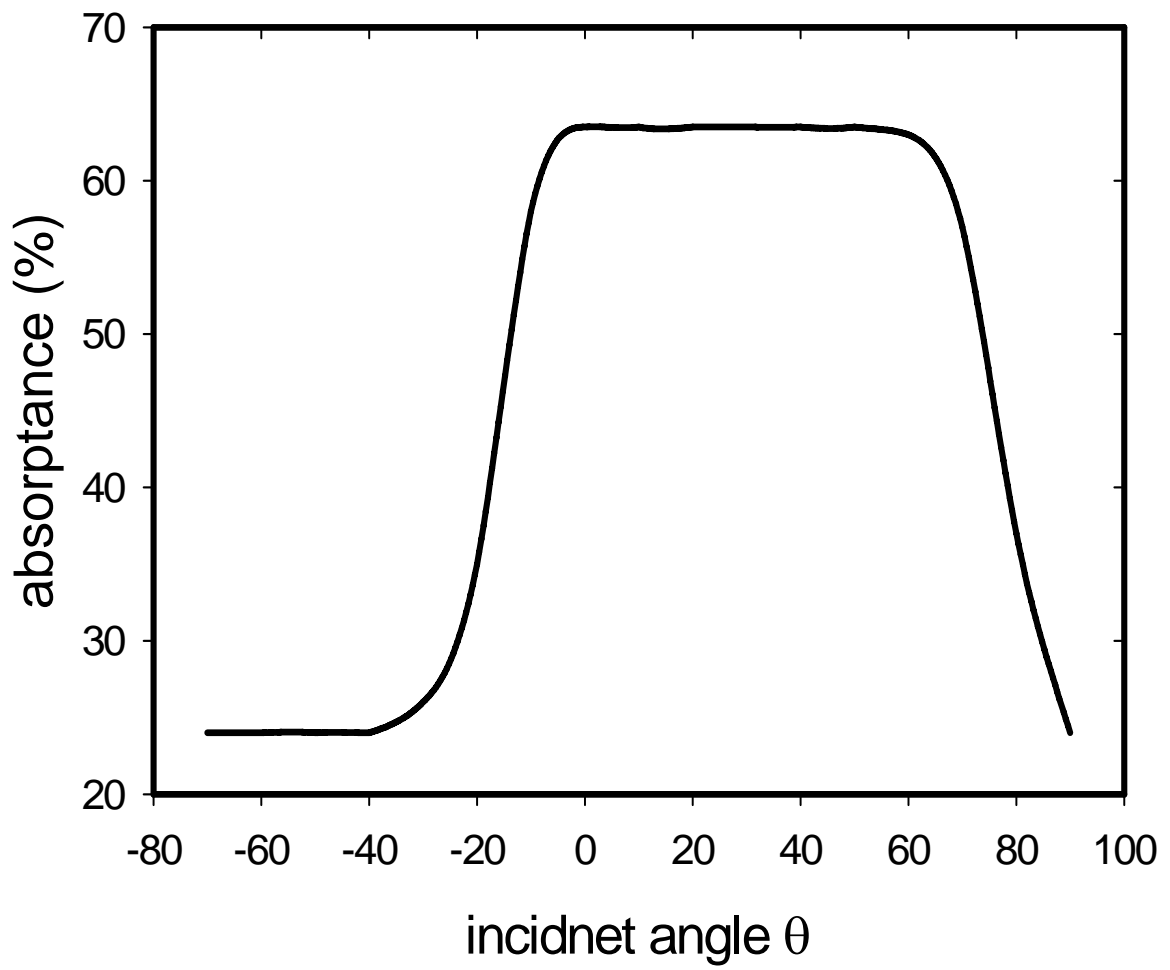


Fig. 3-7 The relation of absorptance and incident angle

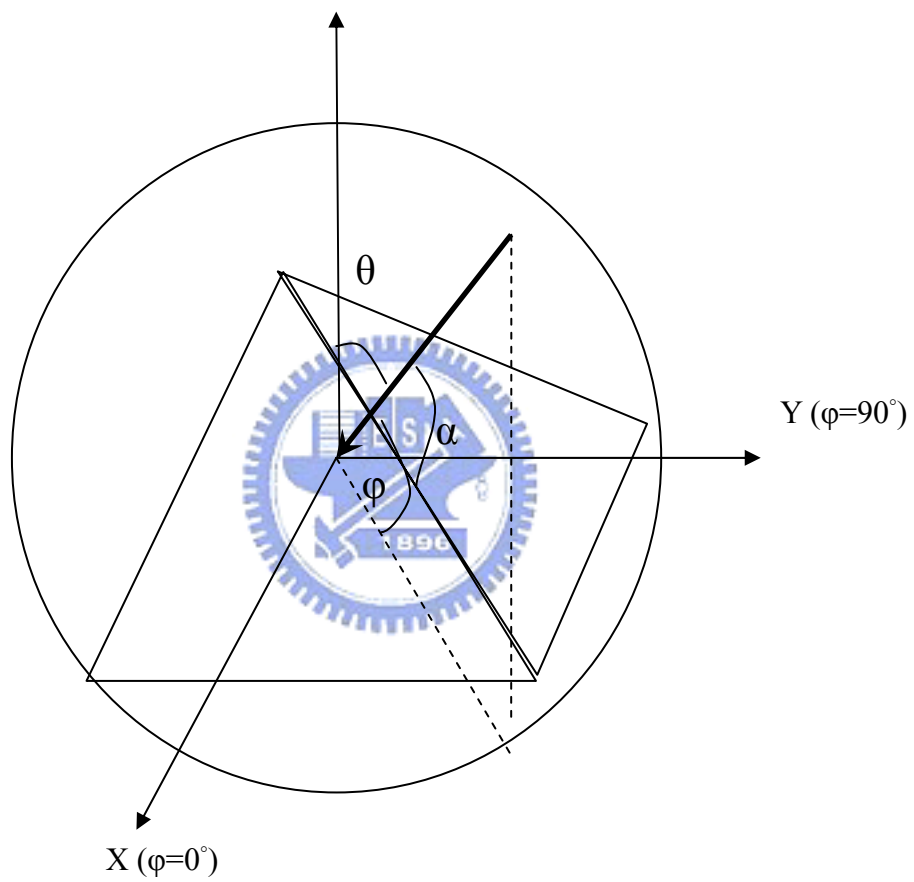


Fig 3-8 The position of the triangle of principal orientations. The incident angle θ and the azimuth angle ϕ are demonstrated.

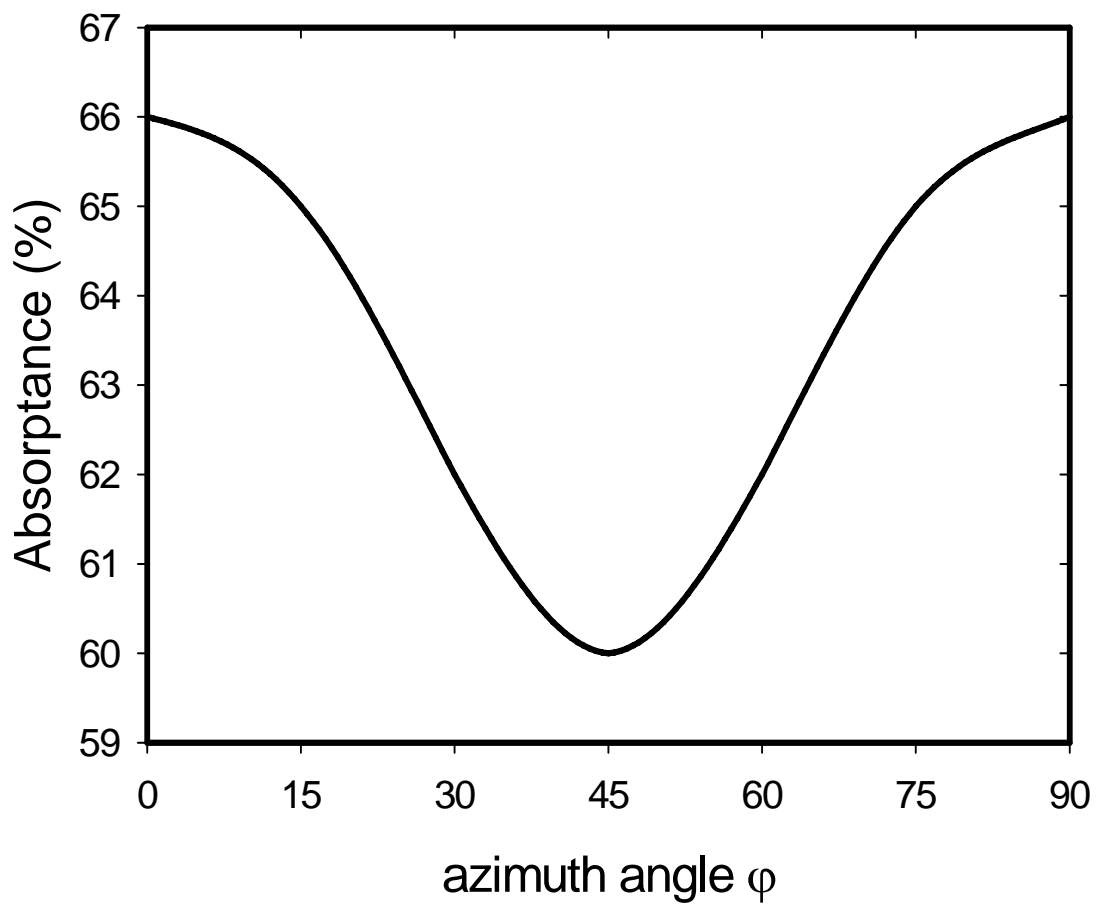


Fig 3-9 The relation between the azimuth angle φ and absorptance

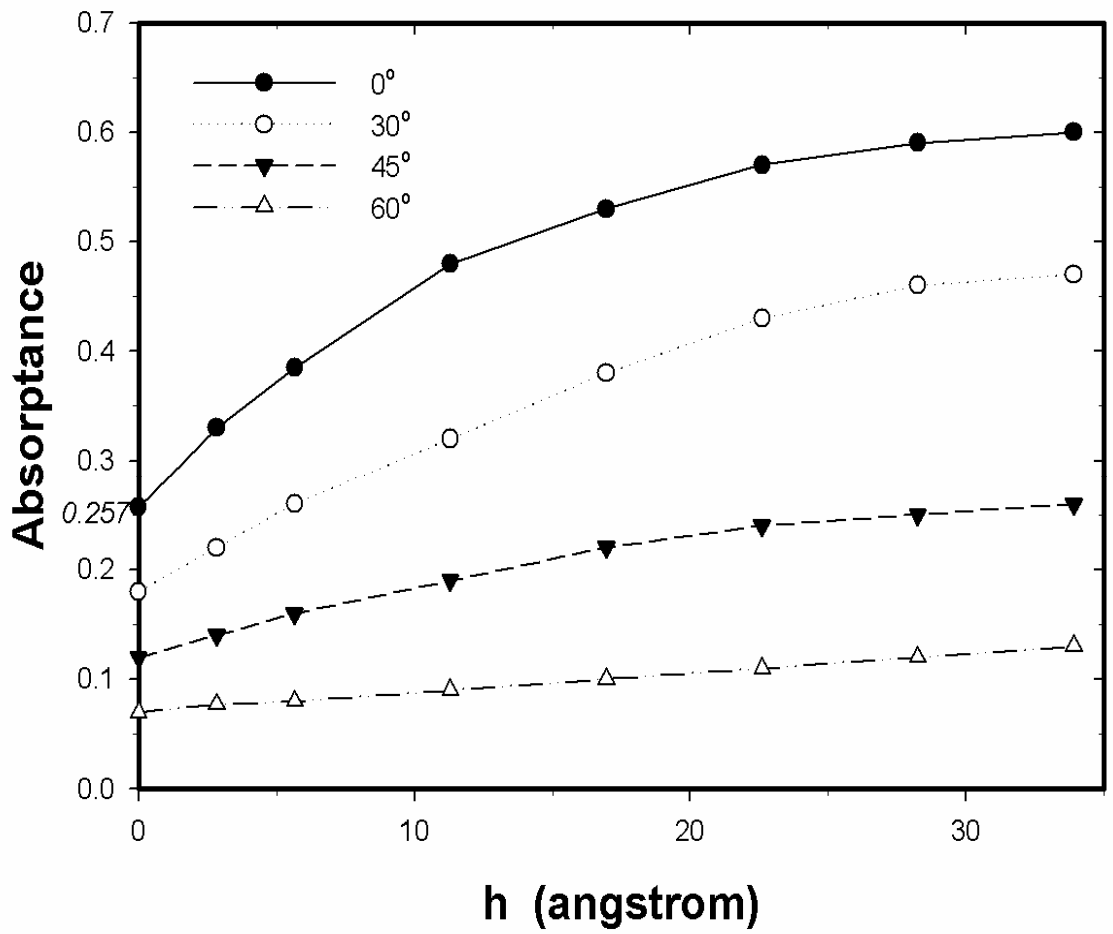


Fig 3-10 The relation among absorptance, h and photon's incidence angle θ of GaAs

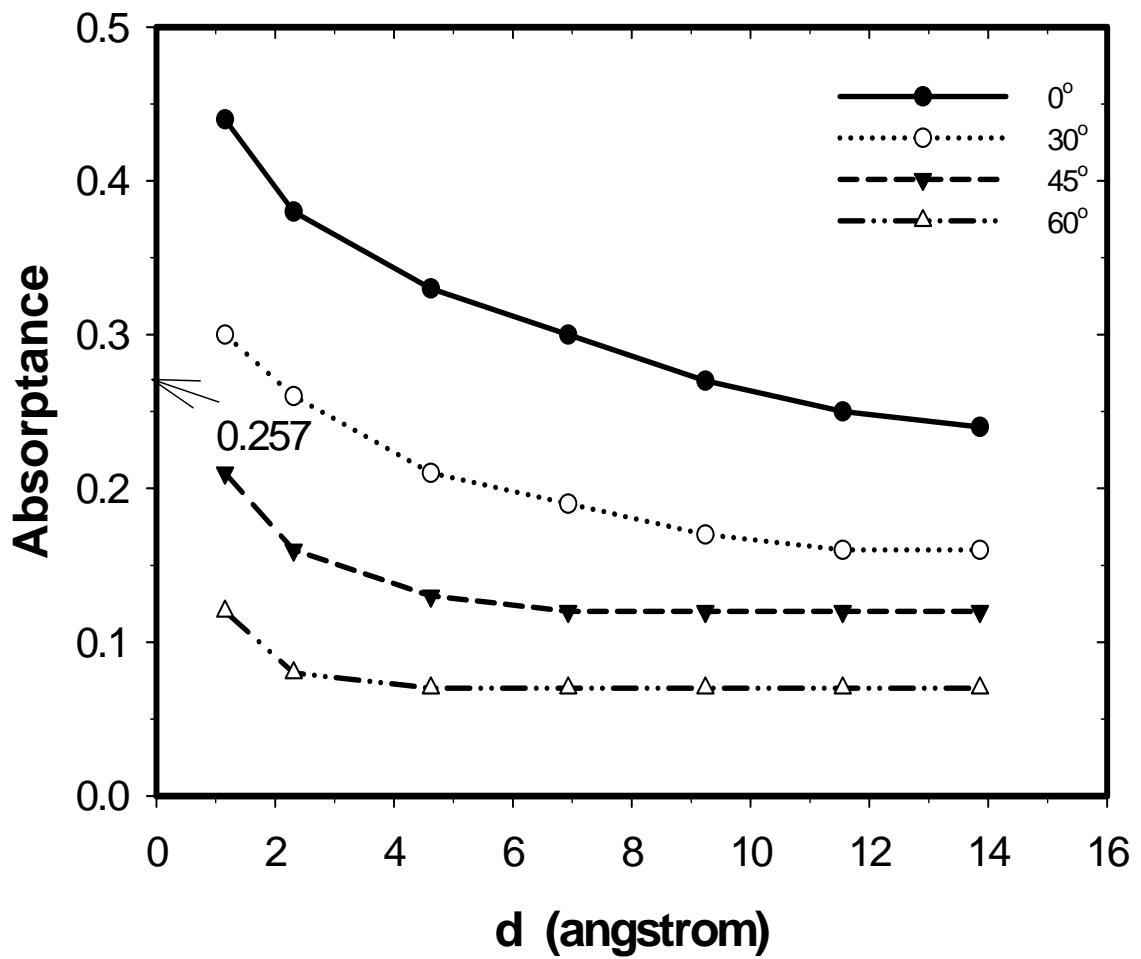


Fig 3-11 The relation among absorptance, distance and photon's incidence angle θ of GaAs

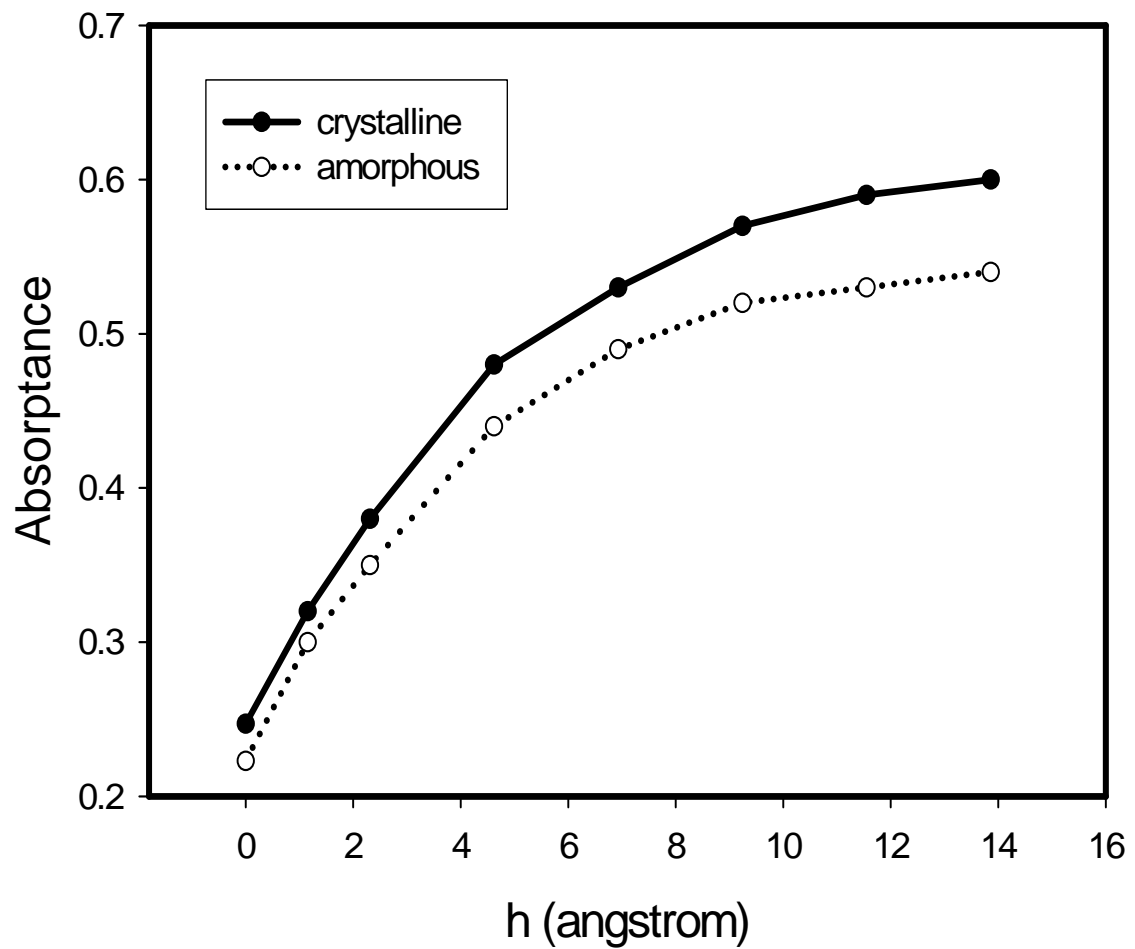


Fig 3-12 The absorbance comparison of amorphous substrate and crystalline substrate in the case of height of square texturing for the square surface case

4. Modified Model with Phonon Emission

The study in chapter 3 did not consider the heat transfer in solar cells. Thus we involve the effect of phonon transmission in our simulations in this chapter.

First of all, three models of Lennard-Jones potential were established. Fig 4-1 shows the three models. The first model is,

$$U(r) = 4 \left[3.86 \left(\frac{1}{r} \right)^{12} - \left(\frac{1}{r} \right)^6 \right] \quad (4-1)$$

Then if we set $r \rightarrow 2r$ and $r \rightarrow 0.5r$, so the second and third model is respectively

$$U(r) = 4 \left[3.86 \left(\frac{1}{2(r-r_0)} \right)^{12} - \left(\frac{1}{2(r-r_0)} \right)^6 \right] \quad (4-2)$$

$$U(r) = 4 \left[3.86 \left(\frac{1}{0.5(r+r_0)} \right)^{12} - \left(\frac{1}{0.5(r+r_0)} \right)^6 \right] \quad (4-3)$$

where r_0 is the distance of zero energy. The distance of repulsive-attractive force is changed. The nondimensional distance of force field (r^*) of model 1 is close to 3; r^* of model 2 is shorter to 2 and r^* of model 3 is almost to 4. That means different phonon emission if we use these three models on the relaxation of Si substrate. In the view of radiation, the longer distance of field r^* represents shorter mean free path of phonons, and more probability of collisions among phonons.

First of all, we make a simulation for plate substrate without involving these three potential models. The absorptance obviously decreased comparing with the model without acoustic transmission among atoms. That means a part of energy was lost by phonon.

Actually, the thickness of a bulk solar cell is usually greater than 0.5mm. If we do simulation with 0.5nm, the numbers of atoms will reach over 100 billions. This is no significant in MD simulations. So the simulations were made to determine the optimal

thickness in this study, showed in figure 4-2. The absorptance maintained at 0.1907 when the numbers of cells over 30, the thickness is over 16.3 nm. Therefore we make a series of simulations with this 30-cell model.

The concept of phonon emission was applied to the simulation of smooth surface substrate, shown in figure 4-3. The absorptances of model 1, 2 and 3 were respectively 0.1907, 0.2122 and 0.1689. Due to the energy loss with phonon emission, the absorptance was lower than that without phonon emission. Besides, shorter phonon's mean free path leads more energy loss, so the absorptance reduced.

Then we applied this model to the simulation of square surface texturization in section 3-1. Figure 2-3 shows the absorptance is 19.07% in perfect surface, obviously lower than the 24.07% of perfect surface without phonon emission. The absorptance also increases with the height of trenches. But the values are apparently smaller than those in section 3-1.

We also applied this model to the simulation of pyramidal surface texturization in section 3.2. Obviously, the trend is similar with the result from the simulation in section 2-3. But absorptance is obviously lower than the value from the simulation without phonon emission. And the values of model 2 are greater than those of model 1 and model 3. The reason is reliable that a part of energy from photon is lost through phonon emission. Nozik [53] have mentioned the absorbed photon energy above the semiconductor band gap is lost as heat through electron-phonon scattering and subsequent phonon emission, as the carriers relax to their respective band edges (bottom of conduction band for electrons and top of valence for holes).

In the results of chapter 3, the values were too higher for a real bulk solar cell. The one of reasons is we didn't consider the heat loss in the energy transformation. The absorptance

even higher than 60% was quite unreasonable. Thus the results from the simulations with phonon emission were close to reality.

Besides, the results with phonon emission also lead to a new thought that the decreasing of heat loss can increase the efficiency of photovoltaic effect. In the mechanism of PV effect, decreasing phonon's transportation is one of feasible direction.



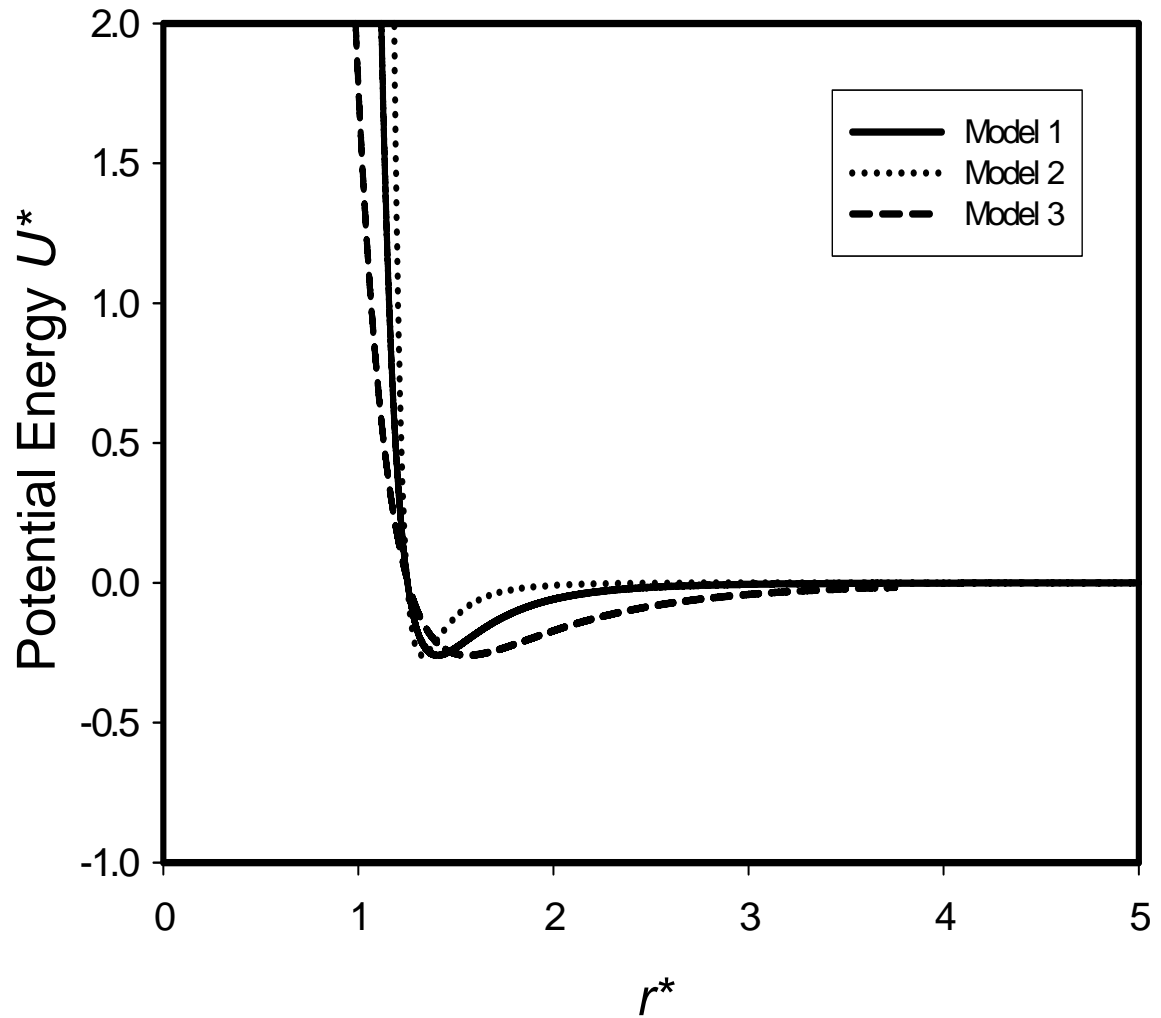


Fig. 4-1 Three models of Lennard-Jones potential. Model 1 is a regular distance effect, and model 2 is shorter distance and model 3 is longer distance.

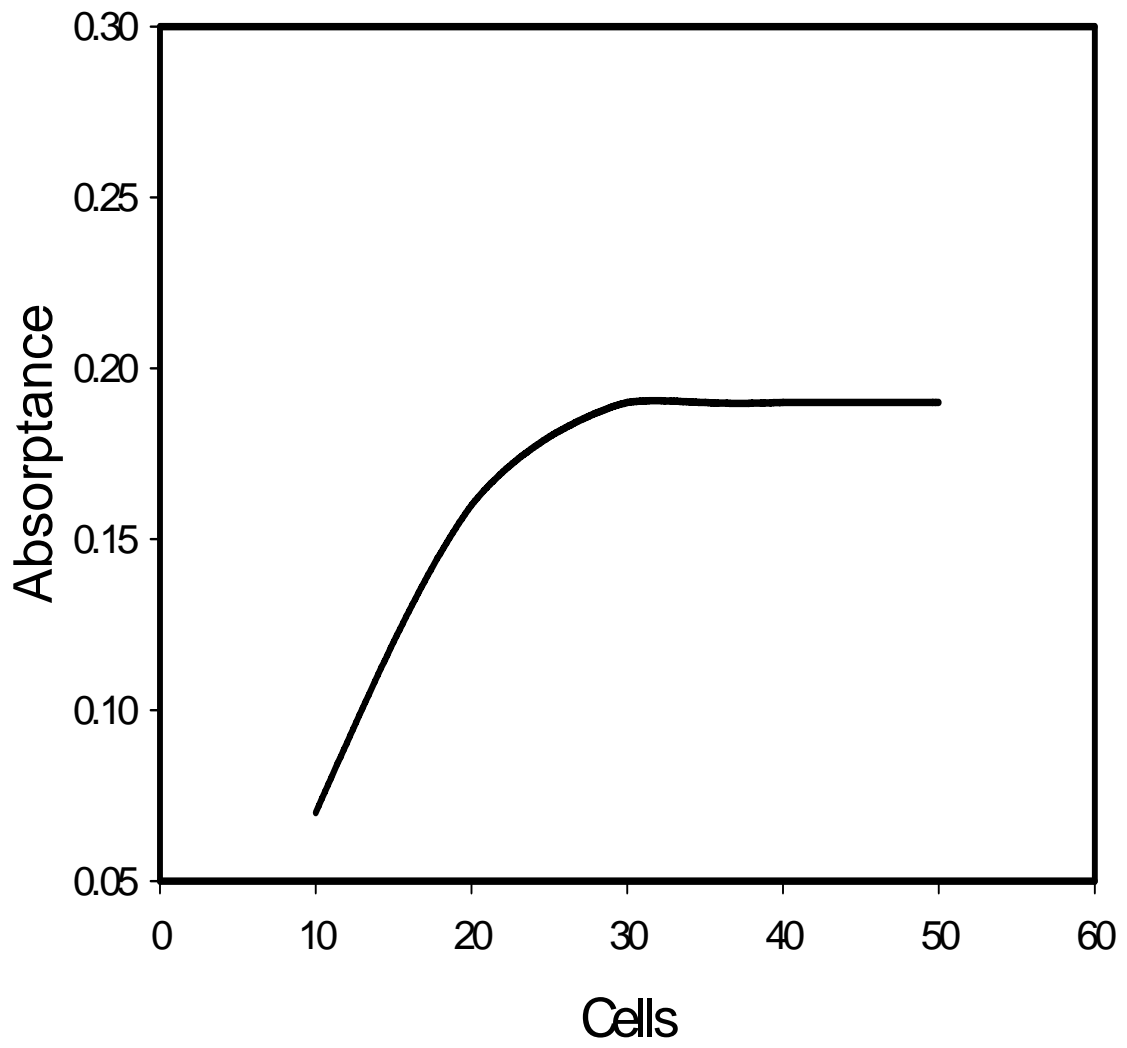


Fig. 4-2 Absorbance via numbers of cells.

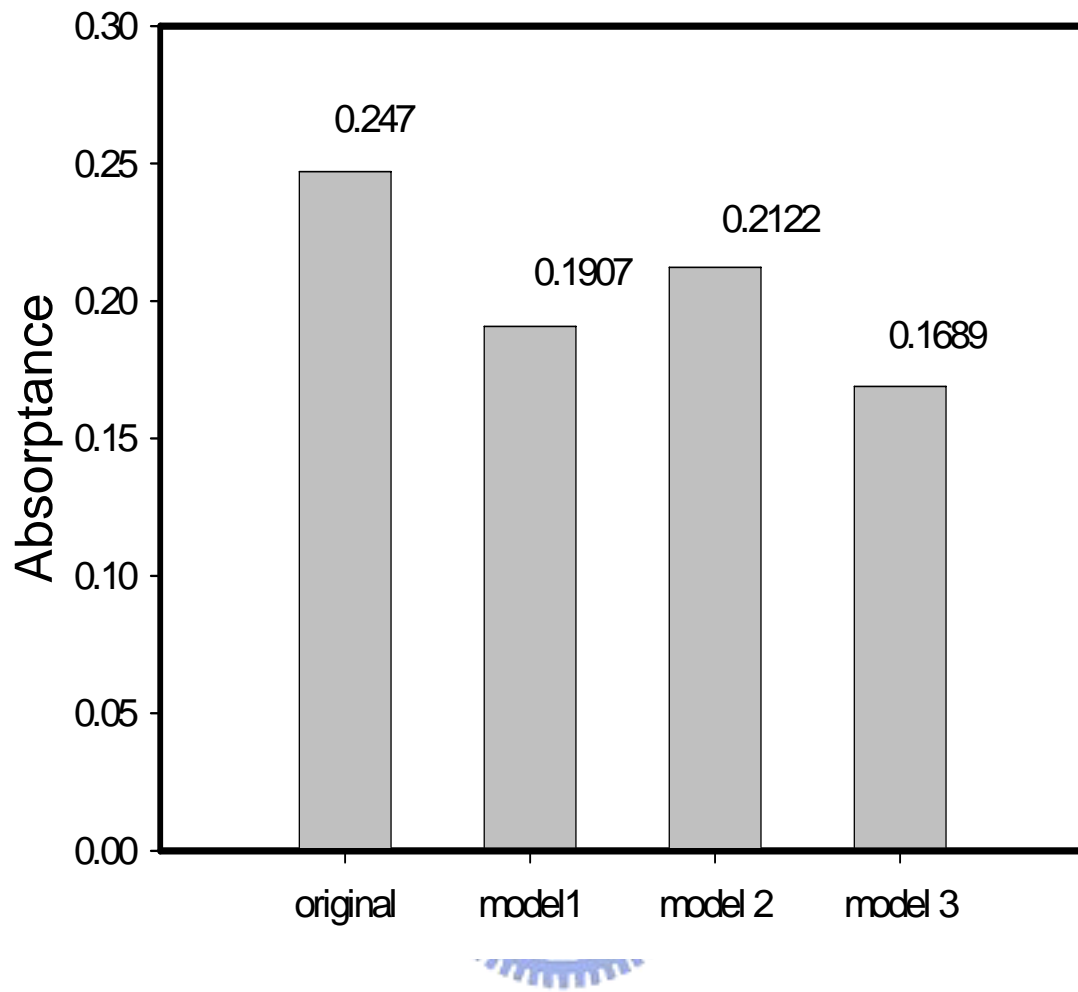


Fig 4-3 The absorbance of original model, model 1, 2 and 3.

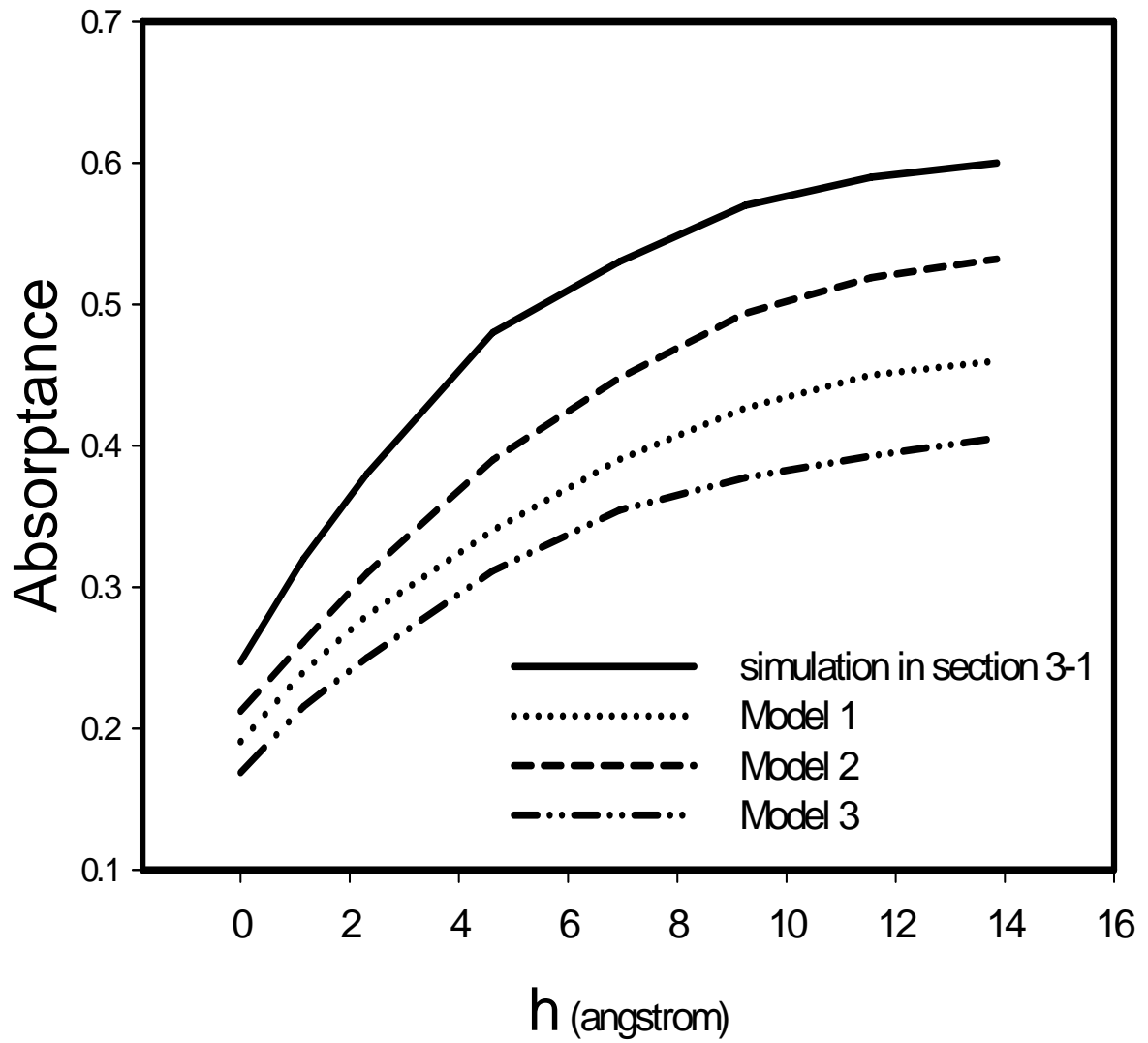


Fig. 4-4 Absorbance via trench's height.

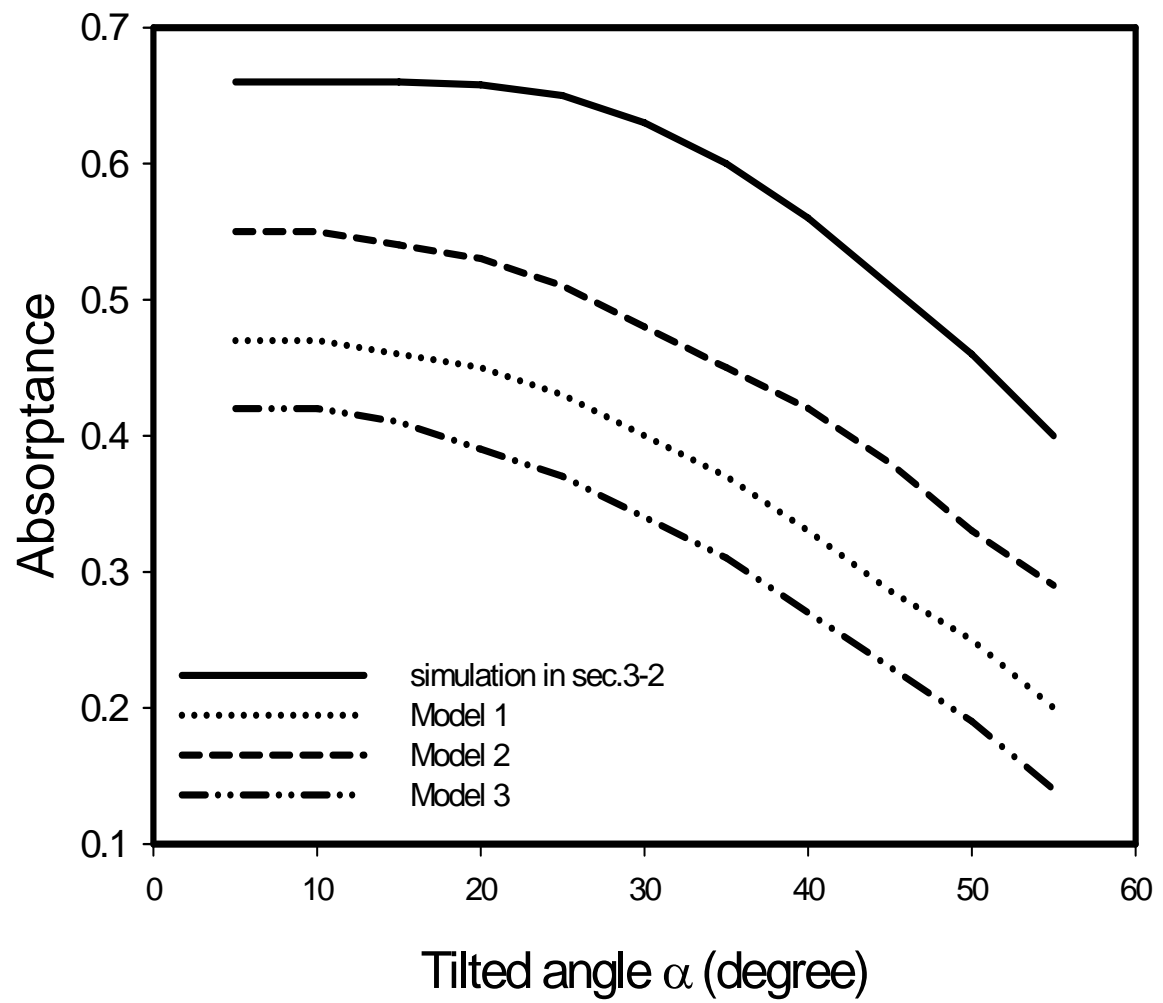


Fig. 4-5 Absorbance via tilted angle in pyramidal surface texturization.

5. Conclusions and Recommendations

In conclusion, this study proposes a new and simple MD model alternative to complex electron-photon interactions in quantum scale to analyze surface texturization of solar cells. Three surface texturization shapes are simulated with various angles of incident light. This methodology can easily determine the absorptance differences of various surface texturizations, and suggest better texturization shapes. In the simulations of mono-crystalline silicon, increasing the trench depth, shortening the distance between two trenches, sharpening pyramids and adding more circling to the semicircular structure all help improve the efficiency of solar cells.

In the case of multi-crystalline silicon by alkaline etching, the large tilted angle leads to the lower efficiency of solar cell. To consider the effect of incident angle, a range of high efficiency exists due to the increasing probability of second reflection. Furthermore, the azimuth angle of incident light also affects the efficiency of solar cells.

In simulations of GaAs solar cells, the effects of square texturization are discussed. As the similar results as that of silicon solar cells, larger square's height and shorter distance between two squares are helpful to increase the probability of second reflection and then enhance the efficiency of solar cells.

From previous studies, we know the emission of heat carriers is an important factor on efficiency. We have interest the effect of phonon emission in our simulation. Thus a modified model with vibration transport among atoms was established. In this model, we found the efficiency of solar cells obviously decreased. The absorptance is 19.07% in perfect surface, obviously lower than the 24.07% of perfect surface without phonon emission. The simulation of trench surface similar with that in section 3-1 shows the absorptance also increases with the height of trenches. But the values are apparently smaller than those in section 3-1.

We also applied this model to the simulation of pyramidal surface texturization in section 3.2. Obviously, the trend is similar with the result from the simulation in section 2-3. But absorptance is obviously lower than the value from the simulation without phonon emission. The reason is reliable that a part of energy from photon is lost to heat sink through phonon emission. Nozik [53] have mentioned the absorbed photon energy above the semiconductor band gap is lost as heat through electron-phonon scattering and subsequent phonon emission, as the carriers relax to their respective band edges (bottom of conduction band for electrons and top of valence for holes)

Our results agree well with previous studies. This MD model can potentially be used to predict the efficiency promotion in any optical reflection-absorption cases.

In the results of chapter 4, we appropriately modified our model with the concept of phonon emission. The absorptance that was higher than 60% decreased to almost 50%. Thus the results from the simulations with phonon emission were close to reality.

Besides, the results with phonon emission also lead to a new thought that the decreasing of heat loss can increase the efficiency of photovoltaic effect. In the mechanism of PV effect, decreasing phonon's transportation is one of feasible direction.

The investigations and findings in previous chapters offer an essential knowledge base for the subsequent study. The next work can be continuously focused on another material, such as InGaP, InGaAs and CdTe *et al.* The more and more potential models are developed, such as different Tersoff potential model for special materials [68, 69]. The other advantage of MD simulations is easily to explore the effect of structures, such as doping, defects and dislocations. Thus we can put the focus on these problems by MD simulations.

To get more precise results, it is necessary to promote the simulation method. Using Monte Carlo method is helpful in our simulations. Monte Carlo method is also helpful to be a contrast to correct our results.

Actually, this MD model is a rough model. Thus, to develop a more precise method is necessary. The method in quantum mechanism such as Born-Oppenheimer Approximation is possible to govern the interaction between photons and electrons in solar cells. If this method can be applied on this problem, this study can make a great contribution to enhance efficiency of solar cells.



Reference

- [1] Z. Xi, D. Yang, W. Dan, C. Jun, X. Li, and D. Que, *Semiconductor Science and Technology* 19 (2004) 485.
- [2] O. Mah, *Fundamentals of Photovoltaic Materials*, National Solar Power Research Institute, Inc., 1998.
- [3] J. M. Damaschke, *Industry Applications*, *IEEE Transactions on* 33 (1997) 1203.
- [4] D. M. Chapin, C. S. Fuller, and G. L. Pearson, *Journal of Applied Physics* 25 (1954) 676.
- [5] J. Nelson, *Physics of Solar Cells*, Imperial College Press: London, 2003.
- [6] Z. I. Alferov, V. M. Andreev, M. B. Kagan, I. I. Protasov, and V. G. Trofim, *Soviet Physics and Semiconductors* 4 (1971) 2047.
- [7] Z. Alferov, *Nobel Lecture* (2000) 413.
- [8] D. C. Reynolds, G. Leies, L. L. Antes, and R. E. Marburger, *Physical Review* 96 (1954) 533.
- [9] A. W. Blakers, A. Wang, A. M. Milne, J. Zhao, and M. A. Green, *Applied Physics Letters* 55 (1989) 1363.
- [10] M. A. Green, A. W. Blakers, and S. R. Weham, in *Proc. 9th E. C. photovoltaic Solar Energy Conference*, 1989, p. 301.
- [11] K. Kuribayashi, H. Matsumoto, H. Uda, Y. Komatsu, A. Nakano, and S. Ikegami, *Japanese Journal of Applied Physics* 22 (1983) 1828.
- [12] Y. S. Tyan, S. Vazan, and T. S. Barge, in *Proceeding 17th Photovoltaic Specialists Conference*, New York, 1984, p. 840.
- [13] M. B. Prince, in *Proc. 8th E. C. Photovoltaic Solar Energy Conference*, Kluwer Scademic, 1988, p. 1632.
- [14] H. F. MacAillan, N. R. Kaminar, M. S. Juryla, M. J. Jadle, D. D. Liu, and G. G. Virshup, in *Proc. 20th IEEE Photovoltaic Specialists Conference*, IEEE, New York, 1988, p. 462.

- [15] Z. Xi, D. Yang, W. Dan, C. Jun, X. Li, and D. Que, *Renewable Energy* 29 (2004) 2101.
- [16] J. D. Hylton, A. R. Burgers, and W. C. Sinke, *Journal of the Electrochemical Society* 151 (2004) G408.
- [17] Y. Nishimoto and K. Namba, *Solar Energy Materials and Solar Cells* 61 (2000) 393.
- [18] U. Gangopadhyay, K. H. Kim, S. K. Dhungel, U. Manna, P. K. Basu, M. Banerjee, H. Saha, and J. Yi, *Solar Energy Materials and Solar Cells* 90 (2006) 3557.
- [19] N. Marrero, B. Gonzalez-Diaz, R. Guerrero-Lemus, D. Borchert, and C. Hernandez-Rodriguez, *Solar Energy Materials and Solar Cells* 91 (2007) 1943.
- [20] M. Lipinski, P. Panek, E. Beltowska, and H. Czternastek, *Materials Science and Engineering B* 101 (2003) 297.
- [21] D. H. Macdonald, A. Cuevas, M. J. Kerr, C. Samundsett, D. Ruby, S. Winderbaum, and A. Leo, *Solar Energy* 76 (2004) 277.
- [22] J. Nijs, S. Sivoththaman, J. Szlufcik, K. De Clercq, F. Duerinckx, E. Van Kerschaever, R. Einhaus, J. Poortmans, T. Vermeulen, and R. Mertens, *Solar Energy Materials and Solar Cells* 48 (1997) 199.
- [23] J. Qian, S. Steegen, E. Vander Poorten, D. Reynaerts, and H. Van Brussel, *International Journal of Machine Tools and Manufacture* 42 (2002) 1657.
- [24] W. A. Nositschka, C. Beneking, O. Voigt, and H. Kurz, *Solar Energy Materials and Solar Cells* 76 (2003) 155.
- [25] M. Spiegel, C. Gerhards, F. Huster, W. Jooss, P. Fath, and E. Bucher, *Solar Energy Materials and Solar Cells* 74 (2002) 175.
- [26] C. F. Li, D. B. Johnson, and R. Kovacevic, *International Journal of Machine Tools and Manufacture* 43 (2003) 925.
- [27] L. A. Dobrzanski and A. Drygala, in 13th International Scientific Conference "Achievements in Mechanical and Materials Engineering" AMME' 2005 Gliwice-Wista, Poland, 2005.
- [28] L. A. Dobrzanski and A. Drygala, *Journal of Materials Processing Technology* 191 (2007) 228.
- [29] B. Tan, K. Venkatakrishnan, and K. G. Tok, *Applied Surface Science* 207 (2003) 365.

- [30] T. Sakoda, K. Matsukuma, Y. M. Sung, K. Otsubo, M. Tahara, and Y. Nakashima, *Japanese Journal of Applied Physics Part 1-Regular Papers Brief Communications & Review Papers* 44 (2005) 1730.
- [31] K. Fukui, K. Okada, Y. Inomata, H. Takahashi, S. Fujii, Y. Fukawa, and K. Shirasawa, in *Technical Digest of International PVSEC-9*, Miyazaki, 1996, p. 93.
- [32] Y. Inomata, K. Fukui, and K. Shirasawa, *Solar Energy Materials and Solar Cells* 48 (1997) 237.
- [33] K. Shirasawa, K. Fukui, K. Okada, Y. Inomata, H. Takahashi, Y. Fukawa, and S. Fujii, in *Proceedings of the 14th EC-PVSEC*, Barcelona, 1997, p. 38.
- [34] H. W. Deckman and J. H. Dunsmuir, *Applied Physics Letters* 41 (1982) 377.
- [35] W. A. Nositschka, O. Voigt, P. Manshanden, and H. Kurz, *Solar Energy Materials and Solar Cells* 80 (2003) 227.
- [36] M. M. D. Ramos and H. M. G. Correia, *Applied Surface Science* 248 (2005) 450.
- [37] W. Stier and O. V. Prezhdo, *Journal of Molecular Structure: THEOCHEM* 630 (2003) 33.
- [38] J. H. Simmons, *Journal of Non-Crystalline Solids* 239 (1998) 1.
- [39] C. Kittel, *Introduction to Solid Physics*, John Wiley & Sons Inc.
- [40] R. Berman, *Thermal Conductivity in Solids*, Oxford Clarendon, 1976.
- [41] M. Sandip and M. Arunava, Vol. 123, ASME, 2001, p. 749.
- [42] J. R. Lukes, D. Y. Li, X. G. Liang, and C. L. Tien, Vol. 122, ASME, 2000, p. 536.
- [43] G. V. Sebastian and C. Gang, Vol. 75, AIP, 1999, p. 2056.
- [44] S. Kotake and S. Wakuri, *Jsmc International Journal Series B-Fluids and Thermal Engineering* 37 (1994) 103.
- [45] S. Volz, J. B. Saulnier, M. Lallemand, B. Perrin, P. Depondt, and M. Mareschal, *Physical Review B* 54 (1996) 340.
- [46] S. Volz, J. B. Saulnier, and M. Lallemand, *Physica B* 220 (1996) 476.
- [47] A. Maiti, G. D. Mahan, and S. T. Pantelides, *Solid State Communications* 102 (1997) 517.

- [48] S. Volz and G. Chen, *Physica B* 263 (1999) 709.
- [49] S. Volz, J. B. Saulnier, G. Chen, and P. Beauchamp, *Microelectronics Journal* 31 (2000) 815.
- [50] S. Volz, J. B. Saulnier, G. Chen, and P. Beauchamp, *High Temperatures-High Pressures* 32 (2000) 709.
- [51] X. L. Feng, Z. X. Li, and Z. Y. Guo, *Microscale Thermophysical Engineering* 7 (2003) 153.
- [52] N. Hirosaki, S. Ogata, C. Kocer, H. Kitagawa, and Y. Nakamura, *Physical Review B* 65 (2002) 134110.
- [53] A. J. Nozik, *Physica E: Low-dimensional Systems and Nanostructures* 14 (2002) 115.
- [54] A. J. Nozik, *Annual Review of Physical Chemistry* 52 (2001) 193.
- [55] R. T. Ross and A. J. Nozik, *Journal of Applied Physics* 53 (1982) 3813.
- [56] D. S. Boudreaux, F. Williams, and A. J. Nozik, *Journal of Applied Physics* 51 (1980) 2158.
- [57] P. T. Landsberg, H. Nussbaumer, and G. Willeke, *Journal of Applied Physics* 74 (1993) 1451.
- [58] S. Kolodinski, J. H. Werner, T. Wittchen, and H. J. Queisser, *Applied Physics Letters* 63 (1993) 2405.
- [59] M. A. Green, K. Emery, D. L. King, Y. Hishikawa, and W. Warta, *Progress in Photovoltaics* 15 (2007) 6.
- [60] A. Rahman, *Physical Review* 136 (1964) A405.
- [61] C. W. Gear and D. S. Watanabe, Vol. 11, *Society for Industrial and Applied Mathematics*, 1974, p. 1044.
- [62] C. W. Gear and K. W. Tu, Vol. 11, *Society for Industrial and Applied Mathematics*, 1974, p. 1025.
- [63] L. Verlet, *Physical Review* 159 (1967) 98.
- [64] S. Gupta, *Computer Physics Communications* 48 (1988) 197.
- [65] A. A. Chialvo and P. G. Debenedetti, *Computer Physics Communications* 60 (1990) 215.

- [66] A. A. Chialvo and P. G. Debenedetti, *Computer Physics Communications* 64 (1991) 15.
- [67] J. Boris, *Journal of Computational Physics* 66 (1986) 1.
- [68] J. Tersoff, *Physical Review B* 39 (1989) 5566.
- [69] D. Powell, M. A. Migliorato, and A. G. Cullis, *Physical Review B (Condensed Matter and Materials Physics)* 75 (2007) 115202.
- [70] P. Vashishta, R. K. Kalia, J. P. Rino, and I. Ebbsj, *Physical Review B* 41 (1990) 12197.
- [71] J. S. Wang, J. Wang, and J. T. Lu, *European Physical Journal B* 62 (2008) 381.
- [72] J. Pozela, A. Namajunas, K. Pozela, and V. Juciene, *Semiconductors* 33 (1999) 956.



Author

姓名：鍾孝彥

地址：桃園縣八德市大忠街 102 號

學歷：

國立交通大學機械系博士班 87/9~97/7

私立中原大學機械系碩士班 85/9~87/7

國立成功大學機械系學士班 78/9~82/7



List of Publications

Journal Paper

1. Chung, H. -Y. Chen, C. -H. and Chu, H. -S., *Analysis of Surface Texturization of Solar Cells by Molecular Dynamics Simulations*, International Journal of Photoenergy, Volume 2008 (2008), Article ID 540971
2. Chung, H. -Y, Chen, C. -H. and Chu, H. -S., *Analysis of pyramidal surface texturization of silicon solar cells by molecular dynamics simulations*, International Journal of Photoenergy, 2008, in press.

Conference Paper

1. Chung, H. -Y. and Chu, H. -S., *Analysis of Surface Texturization of GaAs Solar Cells by Molecular Dynamics Simulations*, in *The International Conference on Molecular/Nano-Photochemistry (Solar'08)*, 2008: Cairo, Egypt
2. Lin, W. -Y., Chung, H. -Y. and Chu, H. -S., *Effects of Airflow in Unidirectional Flow Type Clean Room with Heat Source on Workbench*, 高效率能源技術研討會, 2004, Hsin-Chu, Taiwan